Fall 2022

Numerical investigations of 2-D magnetic nozzles on pulsed plasma plumes

Joshua Daniel Burch

Follow this and additional works at: https://scholarsmine.mst.edu/masters_theses

Part of the Aerospace Engineering Commons, Electromagnetics and Photonics Commons, and the Plasma and Beam Physics Commons

Department:

Recommended Citation

NUMERICAL INVESTIGATIONS OF 2-D MAGNETIC NOZZLES

ON PULSED PLASMA PLUMES

by

JOSHUA DANIEL BURCH

A THESIS

Presented to the Graduate Faculty of the

MISSOURI UNIVERSITY OF SCIENCE AND TECHNOLOGY

In Partial Fulfillment of the Requirements for the Degree

MASTER OF SCIENCE

in

AEROSPACE ENGINEERING

2022

Approved by:

Dr. Daoru Han, Advisor
Dr. Henry Pernicka
Dr. Serhat Hosder

ABSTRACT

This research presents studies of a novel type of magnetic nozzle that allows for three-dimensional (3-D) steering of a plasma plume. Numerical simulations were performed using Tech-X's USim® software to quantify the nozzle's capabilities. A 2-D planar magnetic nozzle was applied to plumes of a nominal pulsed inductive plasma (PIP) source with discharge parameters similar to those of Missouri S&T's Missouri Plasmoid Experiment (MPX). Argon and xenon plumes were considered. Simulations were verified and validated through a mesh convergence study as well as comparison with available experimental data. Periodicity was achieved over the simulation run time and phase angle samples were taken to examine plume evolution over pulse cycles. The resulting pressure, velocity, and density fields were analyzed for nozzle angles from 0° to 14°. It was found that actual plume divergence was small compared to the nozzle angle. Even with an offset angle of 14° for the magnetic nozzle, the plume vector angle was only about 2° for argon and less than 1° for xenon. The parameters that had the most effect on the vectoring angle were found to be the coil current and inlet velocity.

ACKNOWLEDGMENTS

TABLE OF CONTENTS

Page

LIST OF ILLUSTRATIONS

LIST OF TABLES

1. INTRODUCTION

1.1. MOTIVATION

Pulsed inductive plasma (PIP) thrusters offer significant advantages when applied to interplanetary, cislunar, and manned space missions [1]. These advantages include high specific impulse and relatively high thrust, utilization of a wide variety of *in-situ* fuels, and scalability through pulse frequency. Such mission scenarios require these thrusters to possess reliability during long-term operation and adapt to a wide variety of thrust profiles. Their reliability and performance can be further enhanced through the application of non-mechanical thrust vectoring in the form of a magnetic nozzle. Compared with traditional means of beam steering such as mechanical gimbaling, magnetic nozzles have the advantages of reduction in weight, complexity, and throttle response time.

1.2. MODELING APPROACH

Due to the high-density nature of the plume ejection of the PIP source under investigation [2], a fluid simulation approach has been chosen. Specifically, the fluid simulation software USim® [3], developed by Tech-X Corporation, was used. USim® is a fluid plasma modeling framework that simulates the dynamics of charged fluids or neutrals using structured or unstructured meshes. USim®'s capabilities include solutions of compressible Euler equations for neutral gases, ideal MHD equations for ionized gases, Hall MHD, two-fluid plasma, and Navier-Stokes equations. It also supports the solution of multi-fluid multi-temperature equations for chemically reacting plasmas coupled with full Maxwell's equations.

2. LITERATURE REVIEW

There have been several efforts to reveal magnetic nozzle physics through analytical modeling, numerical fluid/kinetic simulations, and experimental approaches.

2.1. REVIEW OF ANALYTICAL MODELS

Several analytical models were developed to describe conditions for efficient magnetic detachment. Arefiev and Breizman demonstrated an ideal MHD analytic solution for plasma detachment in a magnetic nozzle [4]. Inefficiency of detachment was deemed to be insignificant for a sufficiently long nozzle. Reconnection does not contribute to this inefficiency as it only occurs outside the nozzle in the paraxial case.

Breizman et al. developed an axisymmetric steady-state numerical model for plasma flow in a magnetic nozzle [5]. This model was benchmarked against a previous analytical solution in a paraxial, perfectly-conducting, infinite-length, conical nozzle with good agreement. A cylindrical nozzle case with a vacuum gap separating the plasma and wall, demonstrated plasma detachment from the magnetic field. This model showed much lower plasma density values compared to the Detachment Demonstration Experiment (DDEX). This discrepancy was attributed to the model assumption that the plasma flow does not affect the magnetic field configuration.

Ahedo and Merino developed a 2-D analytic axisymmetric model of supersonic acceleration in a divergent magnetic nozzle [6], and analytical models of plasma expansion using initial values from helicon thruster experimental data [7]. The plasma jet at the nozzle throat was found to be radially nonuniform with respect to density but not potential or kinetic energy. Merino et al. derived two semi-analytical approximations for the two-fluid model for plasma plume expansion into the far region [8]. The ambipolar electric field was observed to have a radial accelerative effect on the ions and increase the divergence

angle. Unphysical effects were observed at infinity using the isothermal limit which hints at an unidentified collisionless cooling mechanism. It was determined that the best way to increase divergence angle was to increase the initial ion Mach number.

2.2. REVIEW OF MODELING/SIMULATION STUDIES

Merino and Ahedo used a 2-D fluid code named "DIMAGNO" to produce a 2-D steady-state model of a diverging magnetic nozzle [9]. The ion and electron streamtubes coincided with the magnetic streamtubes at the edge of the plasma due to an increased electric field perpendicular to the magnetic field. Axial pressure force was seen to accelerate when close to the central axis and decelerate when close to the plasma edge. They modified the DIMAGNO code to include an induced magnetic field [10]. Inlet parameters were taken from helicon plasma thruster (HPT) experimental data. A low magnetic field region was observed near the axis. This result was indicative of a mechanism to cause electron demagnetization using the induced magnetic field and subsequent plasma detachment.

Following these studies, Ahedo and Merino performed an analysis of the detachment mechanisms identified within a propulsive magnetic nozzle [11]. It was determined that diffusion and magnetic stretching are not ideal mechanisms to convergently separate the plasma from the field. Electron demagnetization and electrostatic separation were identified as two ideal mechanisms. They then treated electrons and ions as hot polytropic species [12]. The plasma became hypersonic earlier in the nozzle, keeping ion outward separation down and the jet diverged less. The decrease in pressure and electric forces on these ions resulted in greater detachment of the plasma from the magnetic field.

Merino and Ahedo introduced a plasma-induced magnetic field into the DIMAGNO code [13]. The field enlarged the nozzle aperture and subsequently increased plasma jet divergence. A loss in nozzle propulsive force was determined to result from weakened magnetic fields in the central nozzle region arising from the induced field. They again modified DIMAGNO to include the fully magnetized ions limit (FMIL) and compared it

to the unmagnetized ions limit (UMIL) case [14]. The electric field was parallel in the FMIL case and perpendicular in the UMIL case. The FMIL case had a 15% lower ion velocity at the plasma edge but a slightly larger ion velocity at the axis while showing no ion detachment from the magnetic field while the UMIL ions detached early in the nozzle. This evolution of the DIMAGNO code revealed many interesting phenomena related to magnetic detachment and plume divergence.

A 3-D magnetic nozzle case was also examined by Merino and Ahedo through modifying the two-fluid 2-D model to simulate plasma flow through a 3-D vectorial magnetic nozzle consisting of three circular coils [15]. The plasma was assumed to be at the FMIL and quasineutral, collisionless, and low-beta with Maxwellian, isotropic, isothermal electrons. When the coils had equal current supplied, the plume profile resembled the 2-D axisymmetric nozzle. The more current was delivered to the coils with respect to the solenoid, the greater was the deflection angle, up to the 15° limit with zero solenoid current. Reversing one coils polarity allowed the 15° limit to be exceeded. Increasing the current of the coils and maintaining constant solenoid current allowed for a less divergent plume.

A different study using a modeled HPT source revealed independence of the external plasma environment and the nozzle regions. Jiménez et al. developed a 2-D asymmetric model of plasma flow produced within a HPT and expanded through a diverging magnetic nozzle [16]. The simulation tool used was the hybrid particle-in-cell (PIC) and fluid code HYPHEN paired with DIMAGNO. Xenon gas was used with 350 W of HPT power and a 13.56 MHz frequency. The plasma conditions outside of the thruster did not affect the power deposition inside the thruster tube and near plume regions.

Hu et al. used an axisymmetric full PIC model to simulate magnetic nozzle expansion [17]. A maximum thrust contribution of 10% from the nozzle was measured along with a decrease in ion acceleration as compared to experimental data. These results were compared to a similar 1-D model and it was determined that a 2-D model allows signifi-

cantly more accurate predictions of magnetic nozzle propulsive performance. In addition, the fully kinetic model better approximated electron azimuthal current as compared to a simplified fluid model.

The models so far have used fluid and/or PIC approaches. Zhou et al. developed a kinetic Boltzmann-Poisson model to study steady-state expansion of plasma in a paraxial convergent-divergent magnetic nozzle [18]. Only electron-electron collisions were considered and including these collisions in the model resulted in a unique steady-state solution. In this model, the spatial profile in the convergent region was not affected but did increase density in the diverging nozzle as electrons became trapped. These electrons developed different temperatures and velocity distributions.

2.3. REVIEW OF EXPERIMENTAL STUDIES

Specifically to this study, a PIP source, namely, the Missouri Plasmoid Experiment (MPX) has been experimentally characterized. The MPX utilized field-reversed configuration (FRC) plasma generation to produce an initially magnetically self-contained plume [19]. In MPX, the test article was initially filled with a neutral gas within a bias magnetic field. The neutral gas is pre-ionized and then the primary magnetic field is applied opposite to the bias field. This both fully ionizes the plasma and creates a magnetically contained plasmoid. The benefits of this FRC plasma generation includes not needing an electrode and reduced plasma-wall interaction which may lead to worn components and potential failure. Magnetic field and magnetic flux have been mapped by Pahl et al. in order to study plasma formation [19, 20]. Electron temperatures have been measured using a spectrometer to infer plasma formation time and pressure condition [21, 22]. A few preliminary numerical studies using single particle models, iterative PIC, and circuit simulation models have then been performed to determine the optimal strength ratio between the bias field and

pre-ionizing/fully-ionizing field [23] and the primary loss mechanisms with FRC formation [2, 24, 25]. The numerical simulation campaign presented in this study was based on the operating parameters of MPX.

In addition to these studies on MPX itself, three additional experimental studies were selected with initial conditions and plume source types that could be compared to MPX. Deline et al. performed a plasma detachment experiment using a 200 kW pulsed DC plasma source and a 0.07 T magnetic nozzle [26]. The pulsed plasma washer gun operated at a discharge voltage of 270-300 V and 700 A with pulse lengths of 3 ms. The nozzle consisted of five separate coils operated at a maximum of 40 A each. Measurements of plume density, electron temperature, and ion flux were taken. A significant drop was measured in the vacuum magnetic field while ion current and flow velocity remained relatively constant.

Longmier et al. performed an experimental run of the VASIMR VX-200i helicon plasma source to characterize the axial plasma potential profile [27]. A radio-frequency (RF) generator supplied the VX200i with 30 kW and was operated on argon. The VX200i had a peak magnetic field strength of 0.17 T. An ambipolar electric field was measured and determined to cause ion acceleration up to Mach 4 through an electron pressure gradient. Plasma density and electron temperature were measured in the plume at 1×10^{20} m^{-3} and 9 eV respectively. The plasma potential structure was observed to follow the magnetic field in the nozzle.

Morita et al. conducted a plasma flow control experiment using an extreme-ultraviolet database (DB) laser and a four coil magnetic nozzle [28]. Each plasma pulse had a duration of 9.4 ms and each coil was charged with 500 V and 3 kA with a combined field strength of 0.3 T. A B-dot probe was used to measure the magnetic field evolution. The plasma showed a stronger emission pattern in the cusp region when only three of the four coils are powered. Deflection angles for three and two coils were found to be 20° and 56.7°, respectively.

3. THEORY AND SIMULATION SETUP

3.1. THEORY

Magnetic nozzles work on the principle of opposing magnetic fields. The electrons, and to some extent ions, in a plasma create an induced magnetic field through their motion. This field directly opposes the field generated by the solenoidal coils in the nozzle. This propels the plasma through the nozzle. In addition, these opposing forces confine the plasma in the center of the nozzle. These effects were modeled using the USim$^®$ High Energy Density Plasma (HEDP) package.

First, the Biot-Savart law must be used to calculate the magnetic field strength, B, of a solenoidal coil using Eq. (3.1).

$$B = \frac{\mu_0 N I}{2r} \tag{3.1}$$

where μ_0 is the vacuum permeability constant, N is the number of turns in the coil, I is the coil current, and r is the coil radius. This field was then normalized by permeability of free-space. Next, the four ideal compressible magnetohydrodynamics (MHD) Eqs. (3.2)-(3.5) must be solved along with the entropy conservation Eq. (3.6).

$$\frac{\partial \rho}{\partial t} + \nabla \cdot [\rho \mathbf{u}] = 0 \tag{3.2}$$

$$\frac{\partial \rho \mathbf{u}}{\partial t} + \nabla \cdot \left[\rho \mathbf{u} \mathbf{u}^T - \mathbf{b} \mathbf{b}^T + \mathbb{I} \left(P + \frac{1}{2} |\mathbf{b}|^2 \right) \right] = 0 \tag{3.3}$$

$$\frac{\partial E}{\partial t} + \nabla \cdot \left[(E + P) \mathbf{u} + \mathbf{e} \times \mathbf{b} \right] = 0 \tag{3.4}$$

$$\frac{\partial \mathbf{b}^{\mathrm{p}}}{\partial t} + \nabla \times \mathbf{e} + \nabla \psi = 0 \tag{3.5}$$

$$\frac{\partial S_{\mathrm{e}}}{\partial t} + \nabla \cdot [S_{\mathrm{e}} u_{\mathrm{e}}] = 0 \tag{3.6}$$

These five equations utilize the plasma density, ρ, plasma velocity field, $\mathbf{u}$, time, t, magnetic field, $\mathbf{b}$, electric field, E, pressure of an ideal gas, P, inductive electric field, $\mathbf{e}$, plasma magnetic field induced by the inductive electric field, $\mathbf{b}^{\mathrm{p}}$, numerical corrective term, ψ, electron entropy, S_{e}, and electron velocity, u_{e}.

3.2. SIMULATION SETUP

For the simulations presented here, USim$^{®}$ performed a second order upwind discretization of a non-linear hyperbolic system for arrays of charge state, electric field, current, and resistivity. This was performed using a Riemann solver. The magnetic field and charge were updated. The current was calculated using the least squares gradient method on the magnetic field vector. The electric field was calculated using generalized Ohm's law. This was done through integration using the Bulirsch-Stoer scheme. Finally, explicit time integration was performed using the Runge-Kutta method [29]. The plasmas under investigation are argon and xenon. These plasmas were chosen due to their prior use in experiments performed on MPX. These plasmas were defined in USim$^{®}$ using the following properties: atomic weight of ions, A_r, plasma adiabatic index, γ_p, electron adiabatic index, γ_e, initial number density of ions, n_0, temperature of ions at the nozzle inlet, T_i, temperature of electrons at the nozzle inlet, T_e, inlet velocity of the plasma, v, number density of ions at the nozzle inlet, n_i, resistivity of plasma, R, average charge number of ions, z. The values used for the two plasmas are displayed in Table 3.1.

The plasma adiabatic index was kept the same for both species assuming monoatomic plasma for a constant theta-pinch ratio of 0.29 resulting in a fully-ionized gas [30]. The parameter values were chosen to replicate the conditions within MPX and were compared to literature values [20, 24, 31]. The plasma was pulsed at the nozzle inlet in consecutive 3.3 microseconds cosine dependent cycles. The nozzle inlet diameter is 0.1550 m with a diverging outlet diameter of 0.2925 m. A coil-diameter-to-chamber-diameter ratio of 1.15 was chosen to replicate a nozzle fitted to the end of the MPX quartz chamber. The

Table 3.1. Initial plasma parameters

Parameter	Argon	Xenon
A_r (u)	39.948	131.293
n_0 (m^{-3})	1×10^{21}	1×10^{21}
n_i (m^{-3})	1×10^{22}	1×10^{22}
R (mΩ)	27.5	29
T_e (eV)	3.57	1.70
T_i (eV)	0.086	0.041
v (m/s)	2935.66	1619.32
z	1.8	1.8
γ_e	5/3	5/3
γ_p	5/3	5/3

coil current was kept at 4000 A through all runs with the exception of an extreme case at 14,000 A. This value was chosen due to its feasibility for future laboratory experimentation and for literature comparison [28]. It is noted here that the fluid approach using USim® is able to reveal the effects of induced magnetic fields.

Figure 3.1, shows the mesh grid and boundary conditions (BC) used for the simulations in this study. The nozzle (shown in red) was placed at the chamber exit at y = -0.001 m. The inflow BC was applied at the bottom edge of the thruster at y = -0.1173 m. A no-slip BC was applied along the thruster walls and the edges perpendicular to the thruster. No-inflow BC's were applied on other domain edges. These no-slip and no-inflow boundary conditions were chosen following the suggestions in Marks et al. which showed that using a 2-D fluid plasma Dirichlet (no-slip) BC within a divergent nozzle and a zero-flux (no-inflow) BC on the domain exit matched well with experimental data [32].

All the simulations were run till the physical elapsed time of 5×10^{-4} seconds from the quiet start, except the runs checking periodicity, which ran till about 1×10^{-3} seconds. This simulation runtime corresponds to about 150 cycles of the plasma pulse (frequency of 303,030 Hz) and is long enough to ensure periodicity. A dynamic time step dependent on a Courant–Friedrichs–Lewy (CFL) condition of 0.4 was used to advance each step of the simulations. This time step was constrained to under 1×10^{-8} seconds. This choice of
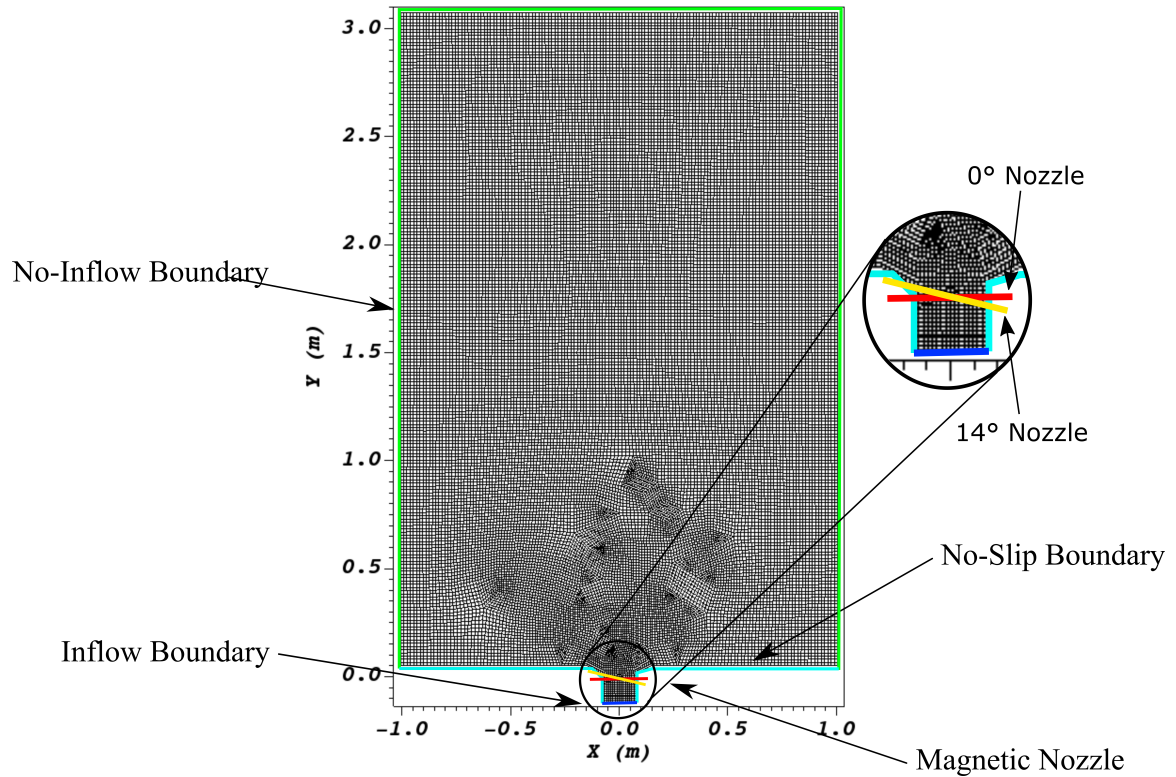
Figure 3.1. Mesh grid used for the simulations. The magnetic nozzle (shown in red) is positioned across the thruster exit at *y* = -0.001 m. The inflow boundary is positioned at the bottom edge of the grid at *y* = -0.1173 m. Axis values are in meters.

CFL number and time step size was based on the consideration of speed of solution and stability of the explicit integration scheme. All runs were performed on a Linux workstation equipped with two 8-core Xeon E5 CPU's with 64 GB of total memory. The runs were performed with an 8-core Message Passing Interface (MPI) configuration with an average computing time for each run of about 2 hours.

4. MODEL VERIFICATION AND VALIDATION

4.1. MESH CONVERGENCE STUDY

A mesh convergence study was performed for four grids. The number of nodes and element lengths for these four mesh grids are listed in Table 4.1. 1-D pressure-versus-distance profiles for argon were taken along the central vertical line of the domain and nozzle ($x = 0$) at the simulation time of 1×10^{-6} seconds and plotted in Figure 4.1. It was shown that the results converged at Mesh 3, which consists of 31,104 elements and 30,005 nodes with a 2-m by 3-m plume expansion domain. To ensure this domain is large enough with Mesh 3, an additional case was ran with an enlarged domain (doubled in both directions, 4-m by 6-m plume expansion region) with the same mesh resolution and plotted the 1-D pressure profile on Figure 4.1 as well. Good agreement is shown between large-domain results and small-domain results. Therefore, Mesh 3 with 2-m by 3-m plume expansion domain was used for all runs presented here.

4.2. VALIDATION WITH EXPERIMENTAL DATA

To validate this simulation model and setup using Mesh 3 and the 2-m by 3-m plume expansion domain, the simulation model was ran for a case of simple expansion into vacuum, without a magnetic nozzle (which was the configuration of MPX experiments [33]), and compared results with experimentally measured data [34]. Specifically, electron

Table 4.1. Meshes used in convergence study

Mesh	Nodes	Element Length
Mesh 1	1,943	0.125 m
Mesh 2	7,591	0.0625 m
Mesh 3	30,005	0.03125 m
Mesh 4	119,305	0.015625 m
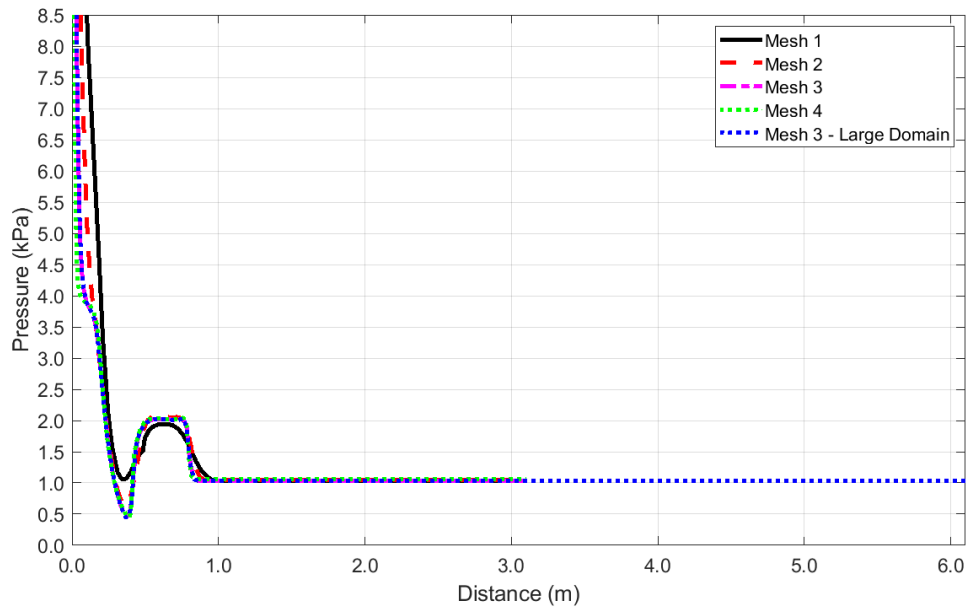
Figure 4.1. Argon pressure along y-axis at $x = 0$ m for the four mesh grids.

temperature T_e was measured in the region downstream of the MPX chamber exit (which is the simulation domain in this study), and was used for direct comparison with our simulation results. Using the coordinates of the simulation domain, the experimental data point chosen for comparison was taken at the location of ($x = 0$ m, $y = -0.1173$ m), which is also the inlet of the simulation domain. From the simulation, T_e history at four points just downstream of the inlet were also sampled over the simulation time period of 5 to 40 microseconds. These time history data of T_e were plotted in Figure 4.2 below. Good agreement between simulation and measurement was obtained for the location near the domain inlet ($x = 0$ m, $y = -0.1172$ m), where the simulation curve showed characteristic pulsed cycle oscillations. The agreement was also achieved for the other three downstream locations after about 20 microseconds when the pulsed injection propagates downstream. This comparison validated the simulation model and setup.
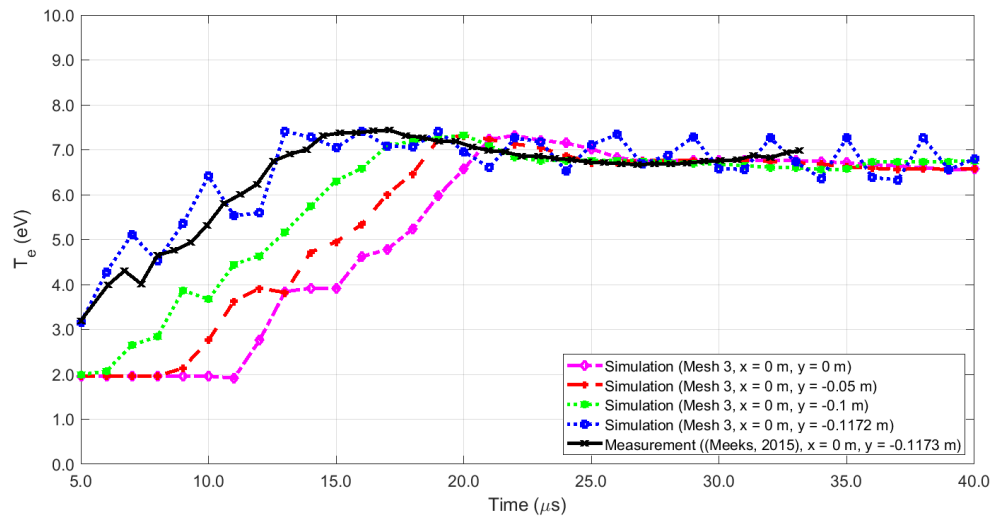
Figure 4.2. T_e at four points in the nozzle region compared with experimental data for flow without an applied magnetic nozzle.

4.3. PERIODICITY OF SIMULATION RESULTS

Pressure values were sampled at a rate of 20 per pulse cycle from the simulation start until periodicity was observed after 1×10^{-3} seconds. The mesh grid origin point was selected as the sample location since it is centered in the magnetic nozzle. These pressure-versus-time plots can be seen in Figures 4.3 and 4.4 for argon and xenon, respectively. For both argon and xenon, the pressure built up and then leveled out. The xenon case took more time to build up pressure due to its larger atomic mass. Periodicity was achieved in approximately the same duration for both gas species.
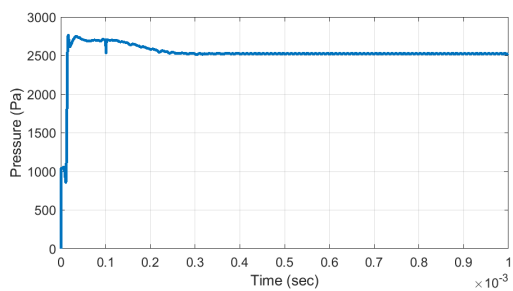
(a) Across 1×10^{-3} seconds and 303 pulses.
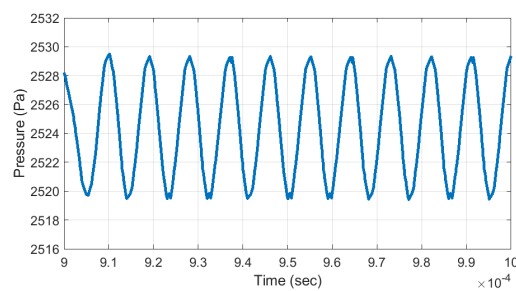
(b) Across 1×10^{-4} seconds and 10 cycles.

Figure 4.3. Pressure vs. time for argon.
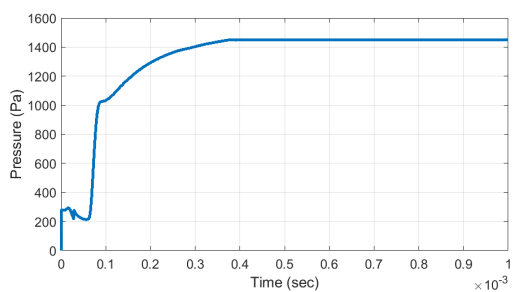
(a) Across 1×10^{-3} seconds and 303 pulses.
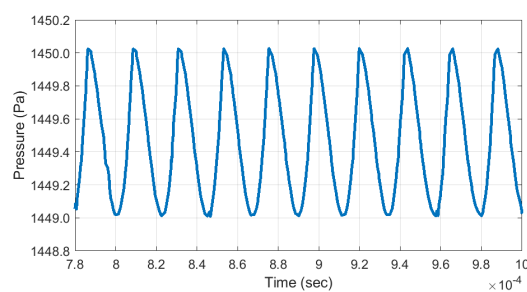
(b) Across 2.22×10^{-4} seconds and 10 cycles.

Figure 4.4. Pressure vs. time for xenon.

5. BASELINE RESULTS

Presented first are baseline results without applying a tilted/vectoring nozzle to check the phase angle values as well as long-time averaged flow field. Both argon and xenon were studied to check the pressure, density, and velocity solutions. Some of the results presented in this thesis can also be found in another publication by Burch et al. [35].

5.1. PHASE ANGLE VALUES

Once periodicity was reached, the phase angles of a cycle were defined as shown in Figure 5.1 with 90° defined at the cycle peak value at the location of nozzle inlet ($x = 0$, $y = 0$). The phase angle variance seen here is limited to the intensity of values at the inlet.

5.1.1. Argon. Pressure, density, and axial velocity were plotted over four phase angles for Argon.

5.1.1.1. Pressure. Figure 5.2 shows argon pressure at different phase angles. At 90° the pressure at the inlet spikes to the highest value of 8,660 Pa. At 270° the lowest pressure of 6,020 Pa occurs at the inlet. Far-field values remain relatively constant. A lobed low pressure region forms directly inline with the nozzle and expands outwards with the plume. These results are similar to those reported in the literature [9, 16].

5.1.1.2. Density. Figure 5.3 shows argon density at different phase angles. Density follows the same pattern as pressure with the highest value of 5.173×10^{-4} kg/m^3 occurring at 90° and the lowest value of 3.418×10^{-4} kg/m^3 occurring at 270°. A similar lobed low density region forms but with stronger gradients bordering the medium density plume. Nuez et al. used a kinetic plume code combined with a two-fluid code to investigate the formation of a high-density region off-axis within the nozzle that follows the magnetic field lines [36]. The results presented here show a high-density region within the plume but with
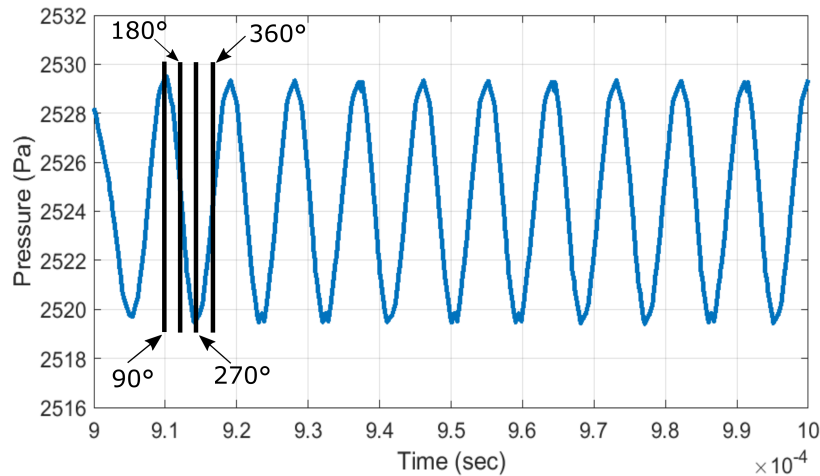
Figure 5.1. Definition of phase angles used for plotting.

a focusing effect towards the axis rather than following the field lines. Merino and Ahedo found that adherence of the plume to the field lines was determined to be a function of the ion magnetization up to the fully magnetized ions limit [14].

5.1.1.3. Velocity. Figure 5.4 shows argon axial velocity at different phase angles. The inlet velocity changes only a few m/s over the phases and the far-field values remain relatively unchanged over this brief time period. The nozzle accelerative effect amounts to a velocity increase of 5,608 m/s over the value at the inlet. A high velocity region forms directly along the plume axis and fans outwards. The nozzle field keeps the plume close to the central axis initially and then allows it to abruptly expand.

5.1.2. Xenon. Pressure, density, and axial velocity were plotted over four phase angles for Xenon.

5.1.2.1. Pressure. Figure 5.5 shows xenon pressure at different phase angles. At 90° the pressure values at the inlet spike to their highest value of 2,427 Pa. At 270° the lowest pressure of 2,310 Pa occurs at the inlet. Far-field values remain relatively constant. A less constricted and roughly trapezoidal low pressure region forms directly inline with the nozzle and expands outwards with the plume. Ahedo and Navarro-Cavallé determined that,

within their nozzle outflow, one of the primary causes of efficiency losses was determined to be incomplete expansion in the nozzle region [37]. Both the argon and xenon cases show a narrowing of the plume at the nozzle exit.

5.1.2.2. Density. Figure 5.6 shows xenon density at different phase angles. Density follows the same pattern as pressure with the highest value of 1.624×10^{-4} kg/m^3 occurring at 90° and the lowest value of 1.481×10^{-4} kg/m^3 occurring at 270°. A similar trapezoidal low density region forms but with stronger gradients bordering the medium density plume with a prominent higher density front, compared with the argon case.

5.1.2.3. Velocity. Figure 5.7 shows xenon velocity at different phase angles. The inlet velocity changes only a few m/s over the phases and the far-field values remain relatively unchanged over this brief time period. The nozzle accelerative effect amounts to a velocity increase of 1,232 m/s over the inlet value. A high velocity region forms directly along the plume axis and fans outwards. Unlike the way argon is constrained from expanding by the nozzle field, the xenon plume is able to expand directly after the outlet.

5.2. LONG-TIME AVERAGED FLOW FIELD

The following long-time averaged flow fields were averaged over a series of approximately 50 pulse cycles from 3.4×10^{-4} to 4.7×10^{-4} seconds with 20 data points per cycle. The long-time averaged flow fields for argon are shown in Figure 5.8. The long-time averaged flow fields for xenon are shown in Figure 5.9. These averages show similar plume profiles as the phase angle values. The long-time averaged fields show no significant difference from the phase angle plots. The same gradients can be seen across the flow fields indicating a gradual and steady increase in all three parameters.

After periodicity is achieved, there is very little difference in pulse cycle phase angle values except for regions near the inlet. These baseline results show steady far-field plume values and constant plume expansion. The nozzle performance can be inferred from the long-time averaged plots. With pulsed operation it is possible to emulate a steady state

thruster plume with a focused ejection pattern. The distinct differences in argon and xenon plumes show that fuel selection is vital in determining thruster performance. Argon resulted in a more focused plume with a greater gained velocity. Xenon showed a less focused and immediately diverging plume that expanded approximately three times slower. The next step is to examine the effects on the plume resulting from offset magnetic nozzles.

(a) 90° phase angle

(b) 180° phase angle

(c) 270° phase angle
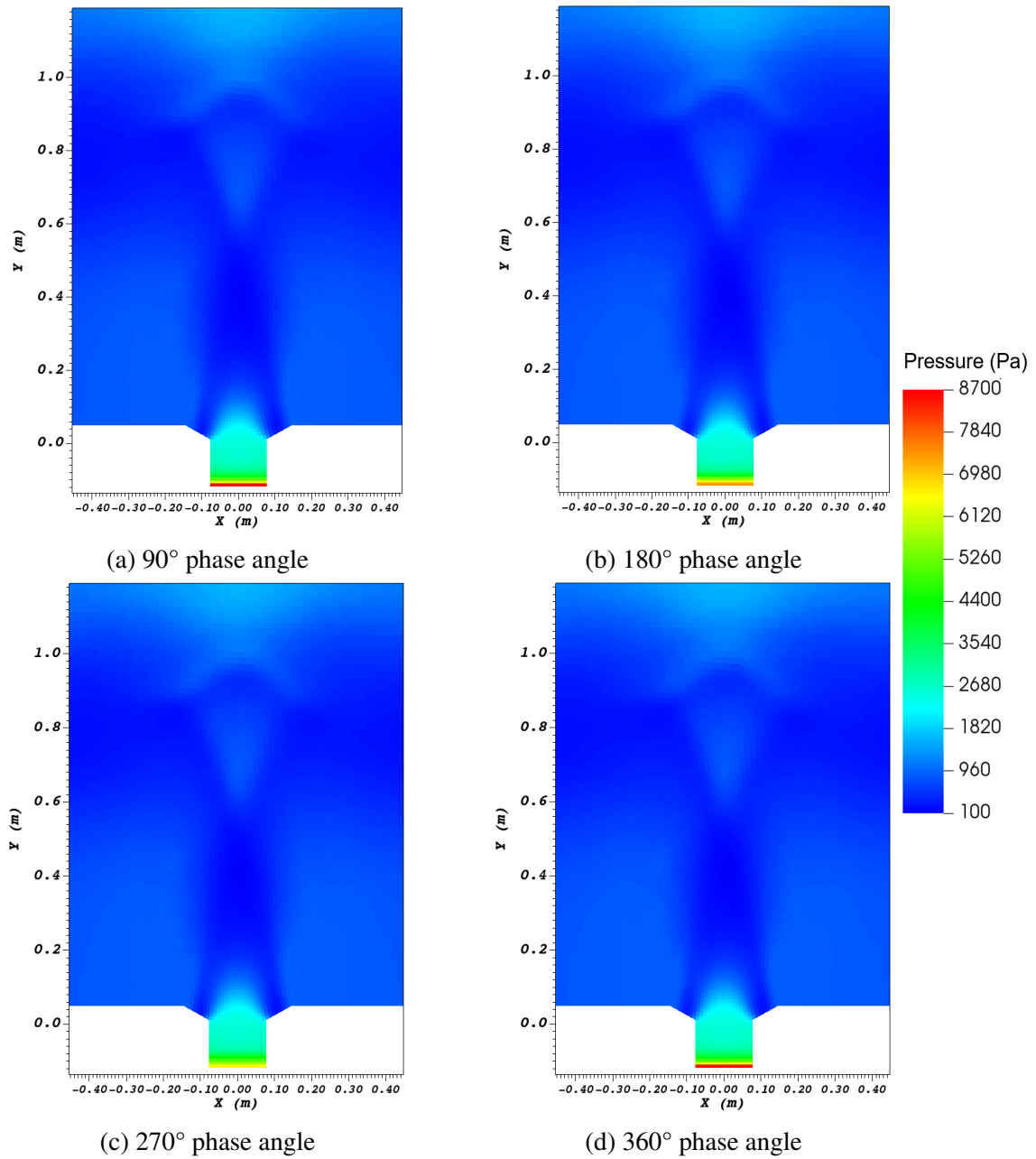
(d) 360° phase angle

Figure 5.2. Pressure in Pa for argon at each phase angle starting at a time of 4.81111×10^{-4} seconds. Zoomed in near nozzle region.

(a) 90° phase angle

(b) 180° phase angle

(c) 270° phase angle
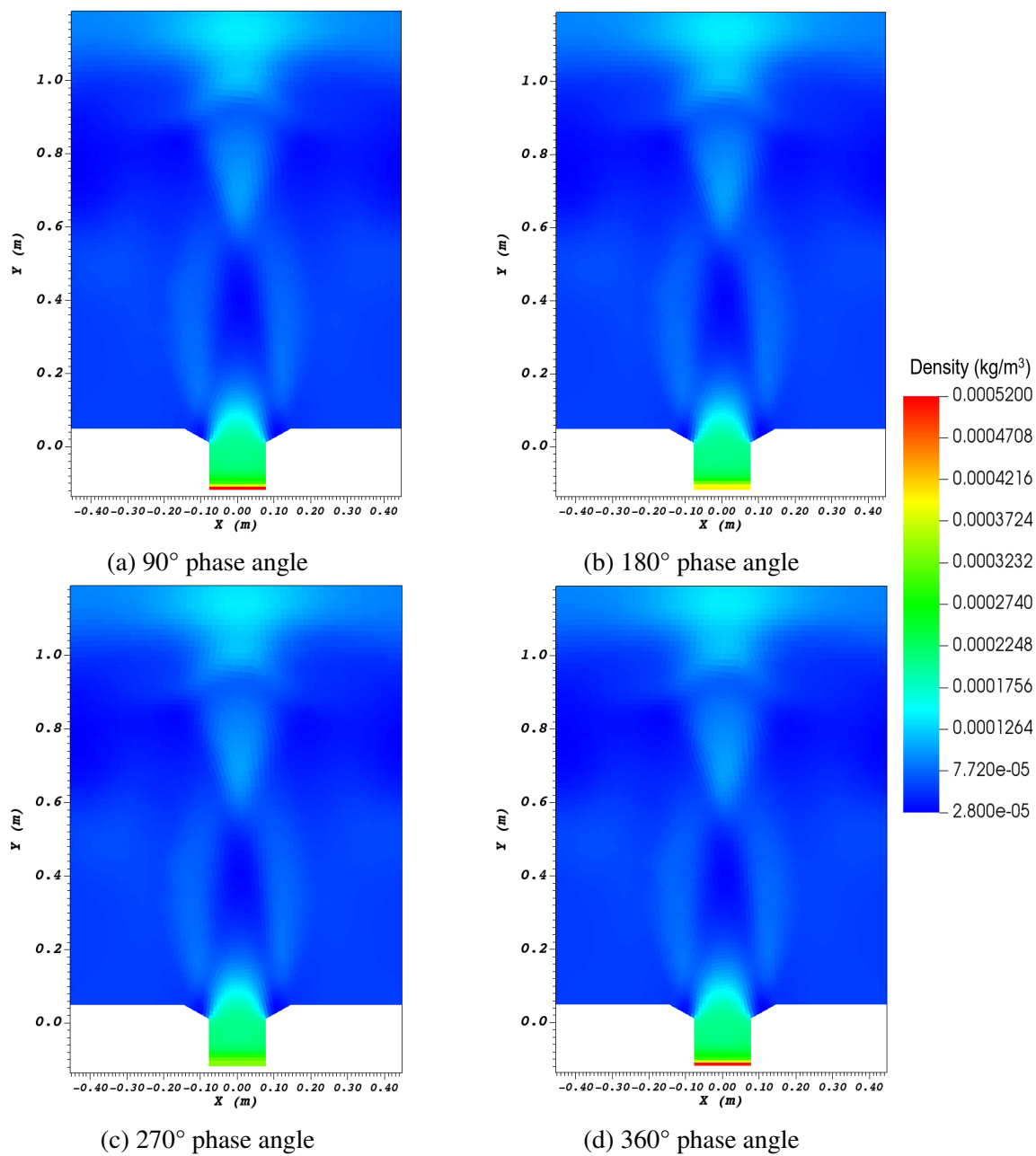
(d) 360° phase angle

Figure 5.3. Density in kg/m^3 for argon at each phase angle starting at a time of 4.81111×10^{-4} seconds. Zoomed in near nozzle region.

(a) 90° phase angle

(b) 180° phase angle

(c) 270° phase angle
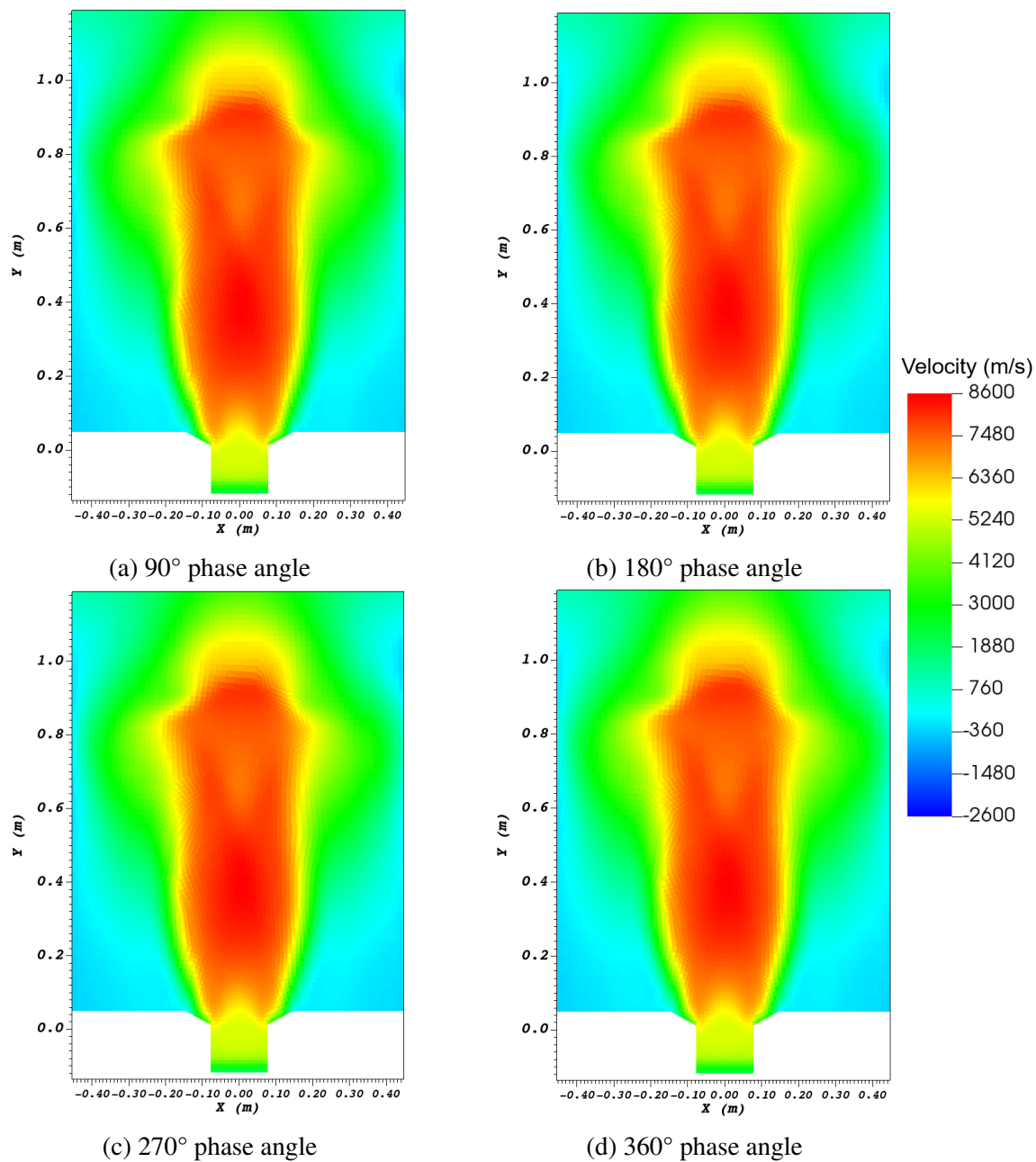
(d) 360° phase angle

Figure 5.4. *y*-velocity component in m/s for argon at each phase angle starting at a time of 4.81111×10^{-4} seconds. Zoomed in near nozzle region.

(a) 90° phase angle

(b) 180° phase angle

(c) 270° phase angle
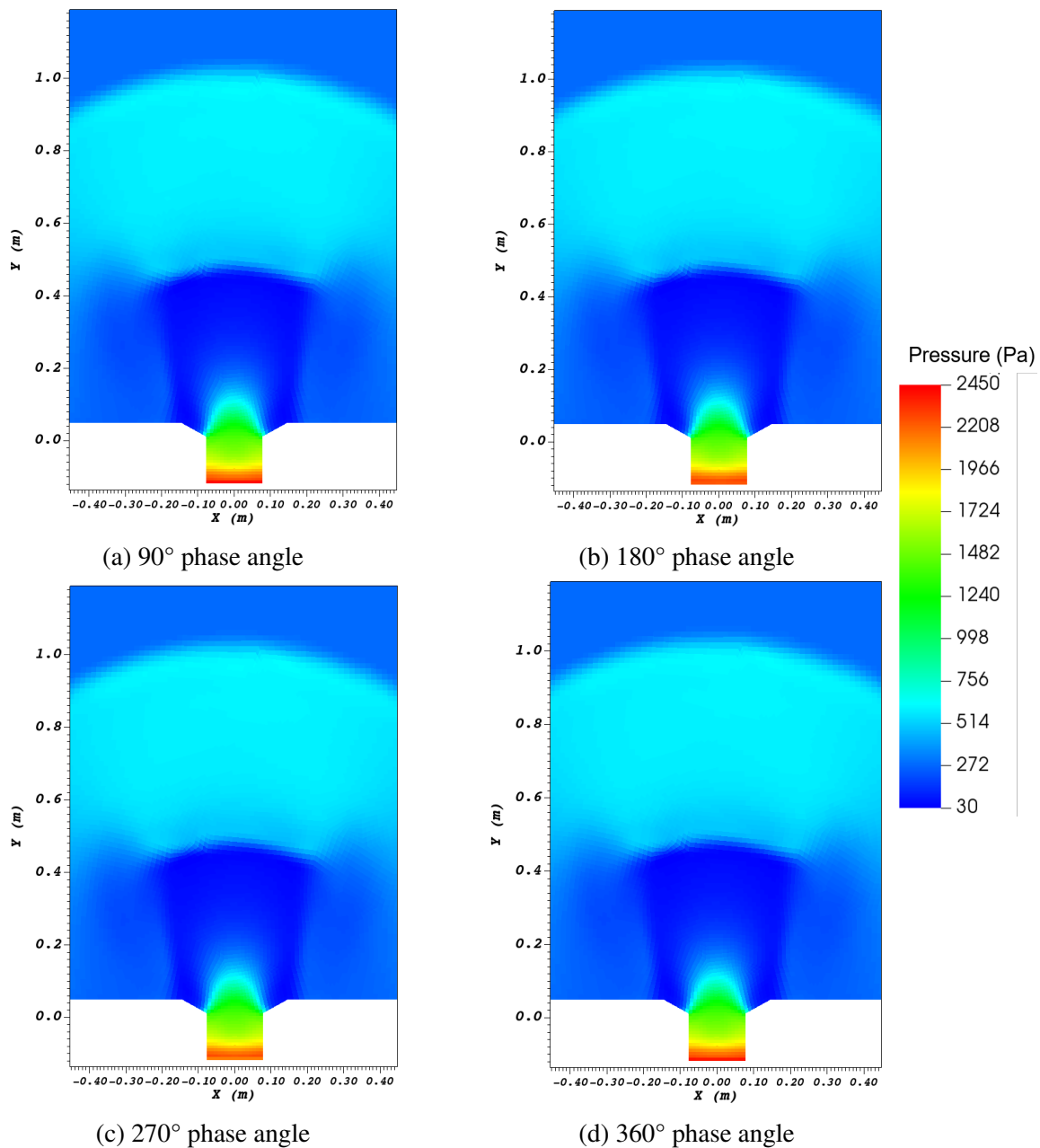
(d) 360° phase angle

Figure 5.5. Pressure in Pa for xenon at each phase angle starting at a time of 4.81111×10^{-4} seconds. Zoomed in near nozzle region.

(a) 90° phase angle

(b) 180° phase angle

(c) 270° phase angle
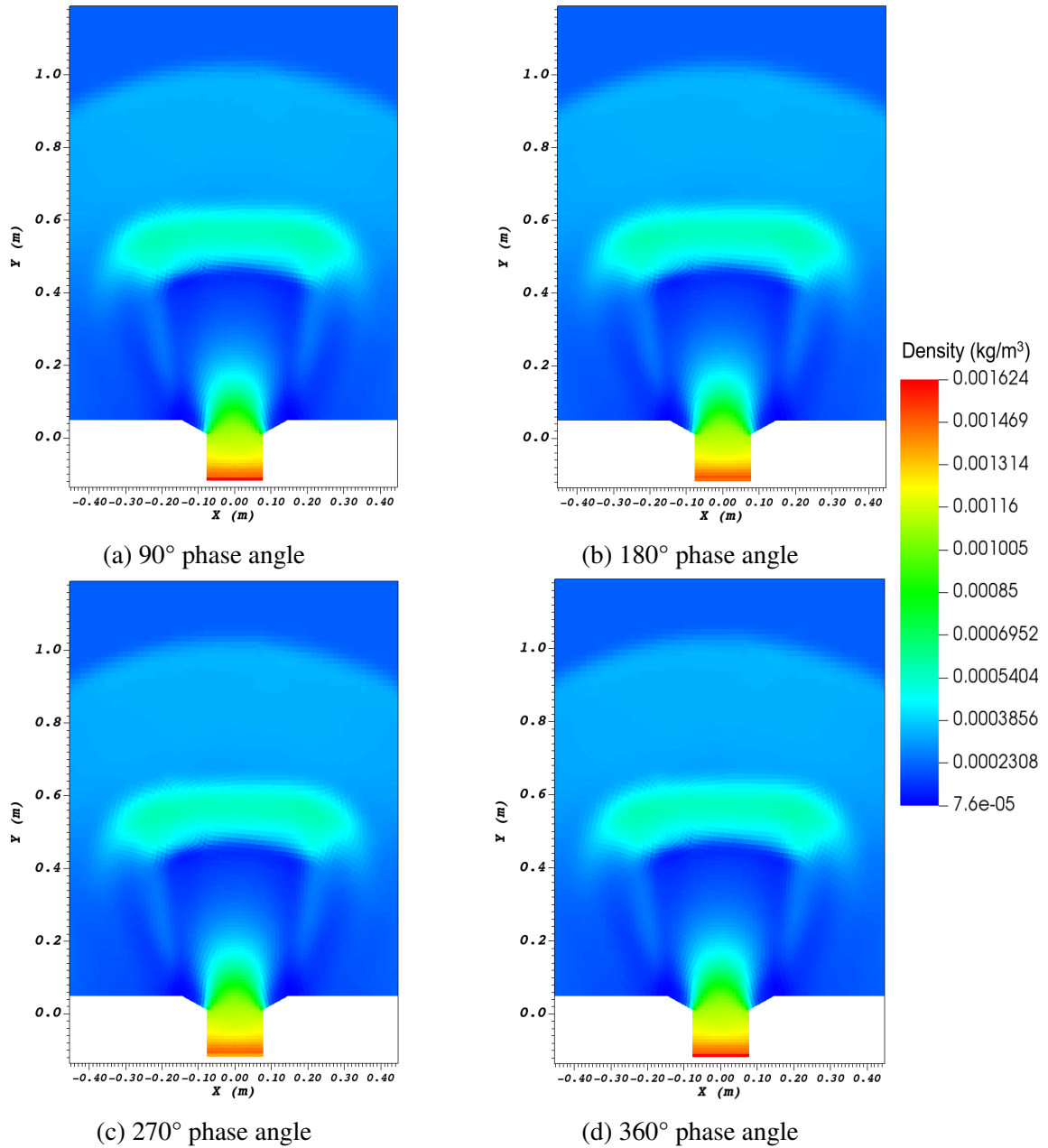
(d) 360° phase angle

Figure 5.6. Density in kg/m^3 for xenon at each phase angle starting at a time of 4.81111×10^{-4} seconds. Zoomed in near nozzle region.

(a) 90° phase angle

(b) 180° phase angle

(c) 270° phase angle
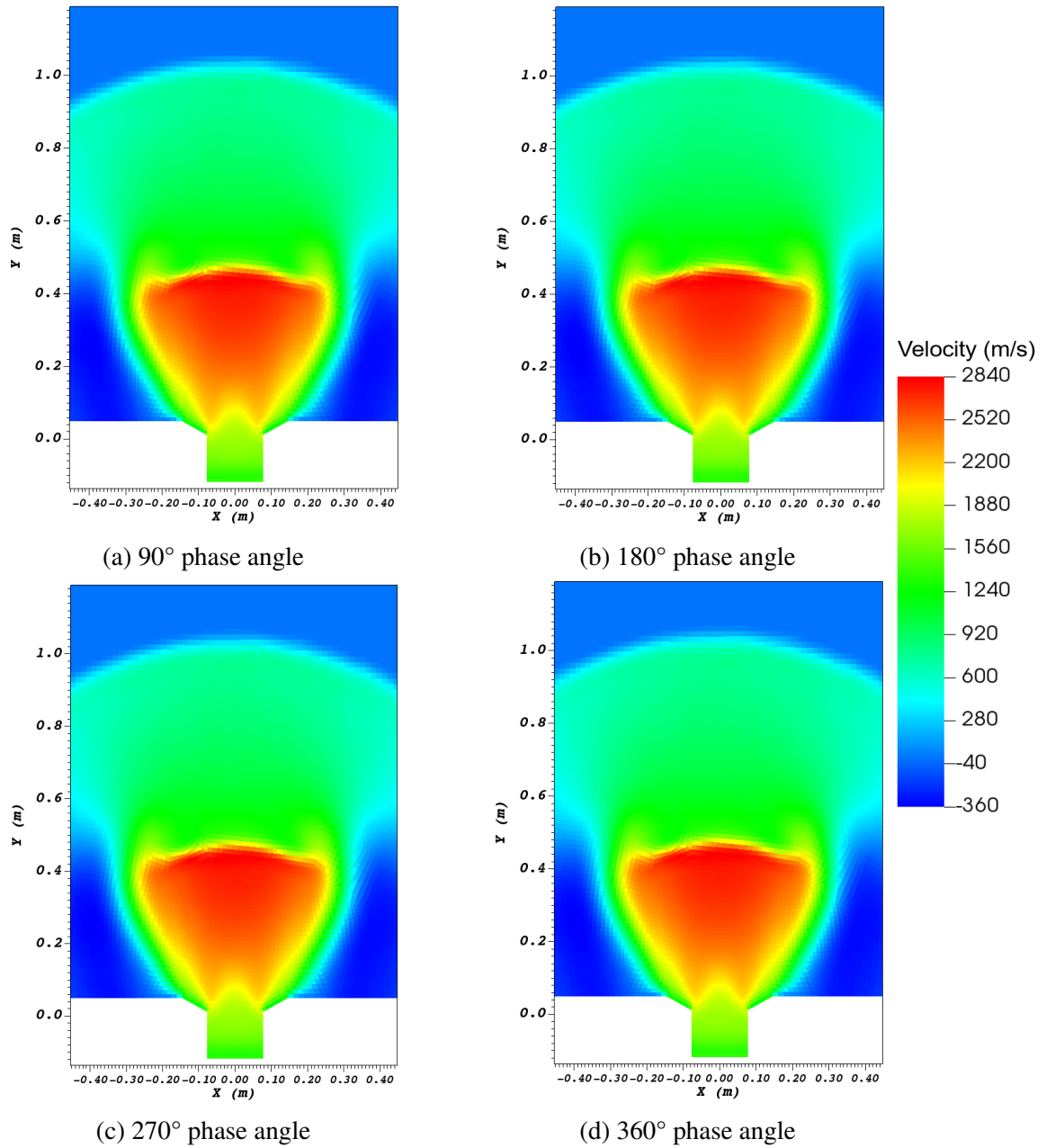
(d) 360° phase angle

Figure 5.7. y-velocity component in m/s for xenon at each phase angle starting at a time of 4.81111×10^{-4} seconds. Zoomed in near nozzle region.

(a) Pressure in Pa

(b) Density in kg/m^3
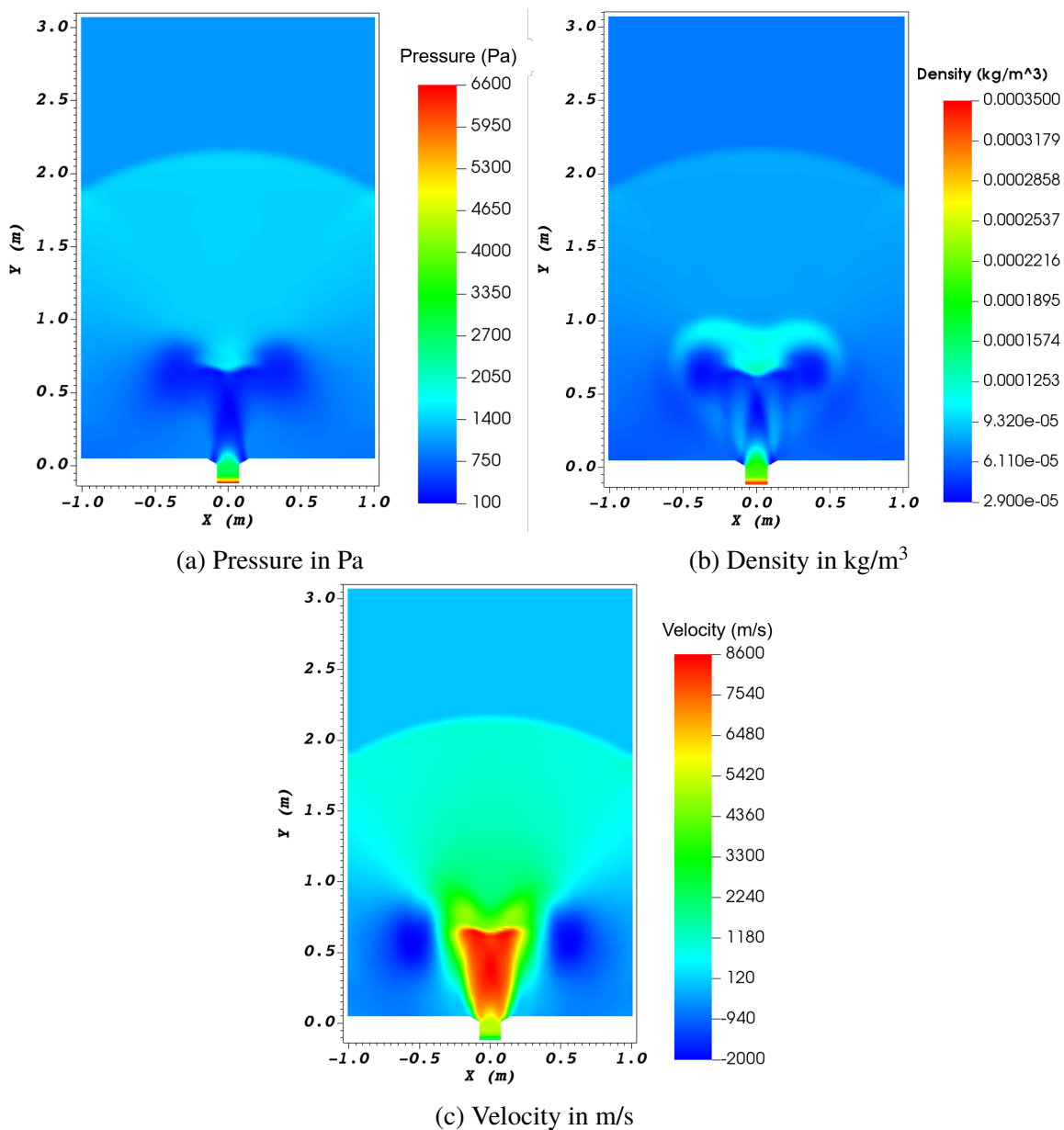
(c) Velocity in m/s

Figure 5.8. Long-time averaged domain pressure, density, and velocity (in the *y*-direction) for argon over 50 pulse cycles.

(a) Pressure in Pa

(b) Density in kg/m^3
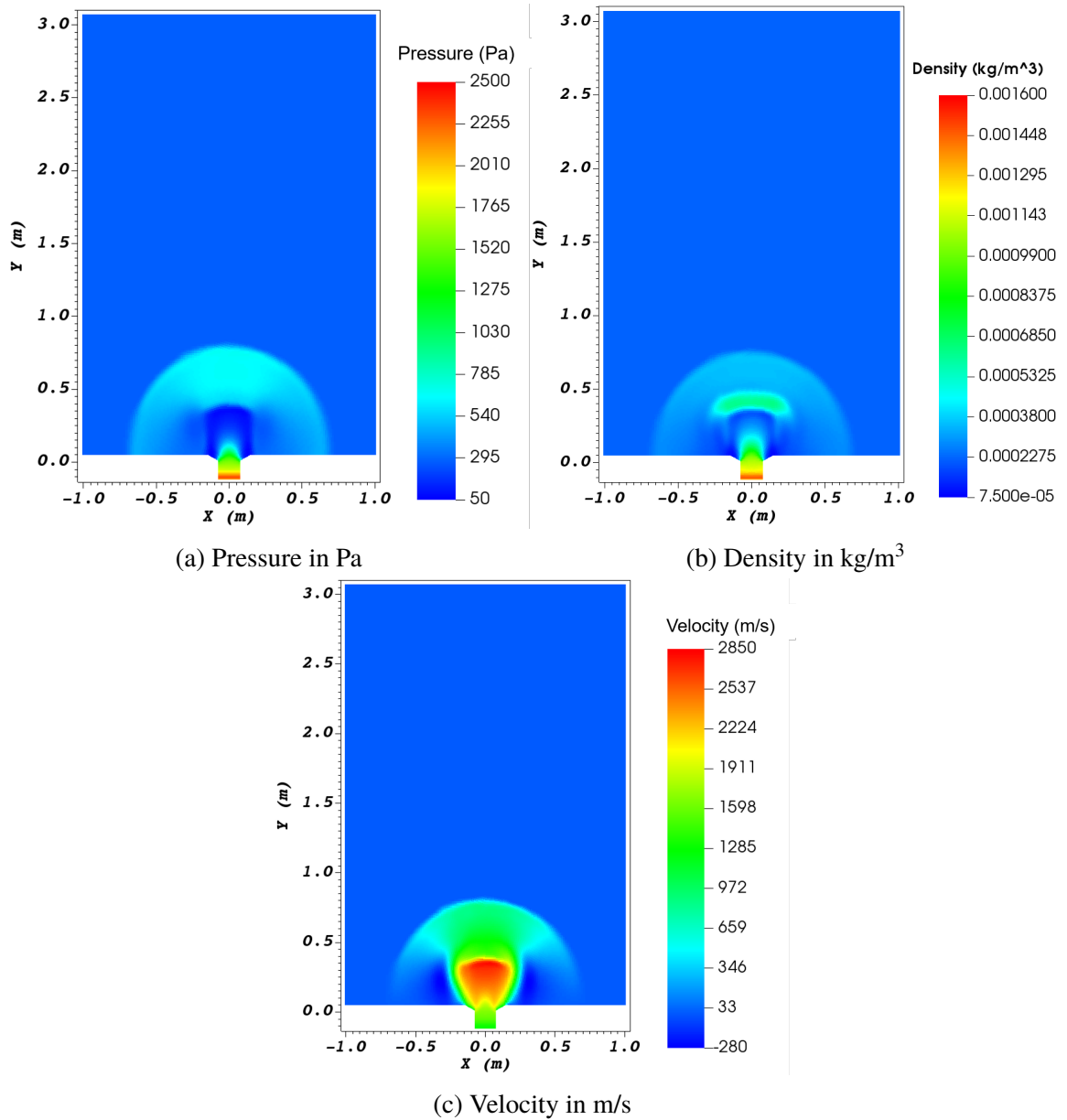
(c) Velocity in m/s

Figure 5.9. Long-time averaged domain pressure, density, and velocity (in the *y*-direction) for xenon over 50 pulse cycles.

6. THRUST VECTORING USING OFFSET NOZZLES

For the simulations with offset (tilted) nozzles, the same inlet parameters were used except for the last three cases discussed in this section. The nozzle was offset (shown in yellow) at angles with respect to the domain *x*-axis as shown in Figure 3.1. Eight runs were performed for both argon and xenon species from 0° to 14° of nozzle offset in 2° increments. Pressure, density, and velocity long-time averaged flow fields were averaged over a series of approximately 30 pulses from 3.4×10^{-4} to 4.7×10^{-4} seconds for all the nozzle angles. The results show little distinction or plume vectoring among angles of 2° through 12°. These additional angles can be found in Figures 1-12 in the appendix. Early work was performed for offset nozzles considering argon, xenon, and hydrogen plumes and using a smaller domain [38].

6.1. ARGON

Figure 6.1 shows the velocity vectors for 14° offset angle at 90° phase angle along with the vector plots of 0° offset for comparison. Two "arms" can be seen curving from the plume back towards the nozzle inlet for both nozzle angles. It can be seen that the plume axis retains its accelerated direction while the plume edges are compelled to remain attached to the field lines. The 14° case shows a visible deflection in the plume "arms" and a bias in velocity magnitudes towards the right side of the plume. These vectors showed an average of 2.32° plume offset for argon. This value was found by averaging all plume vectors with magnitude larger than 6,500 m/s in order to find the vectoring angle of the primary plume region excluding far field values. The argon velocity showed an increase of 5,644 m/s through the nozzle at 14°. These "arms" follow the magnetic field lines and are not seen in the xenon vector plots. It is likely that this phenomenon results from the argon's difficulty in detaching from the field lines at lower velocities. In this case, the requisite velocity for detachment was approximately 4,200 m/s determined by the highest values observed within

(a) Velocity in m/s at 0°

(b) Velocity in m/s at 14°
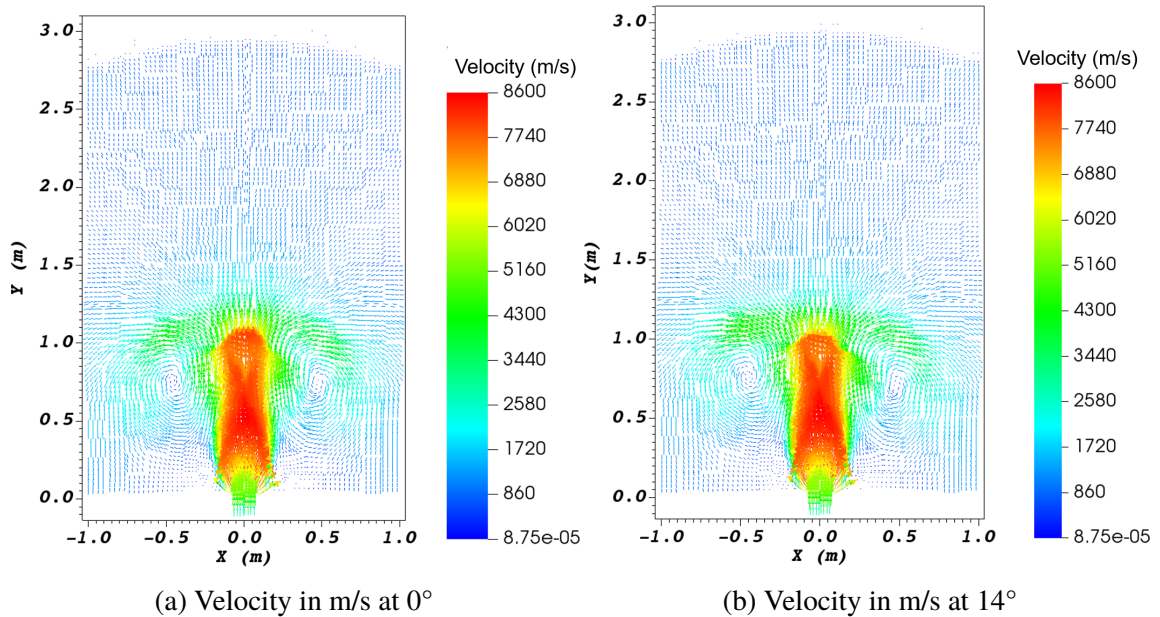
Figure 6.1. Argon velocity vectors at the time of 4.81111×10^{-4} seconds (90° phase angle) for 0° and 14° of nozzle offset (perpendicular to plasma flow).

the plume "arms". Merino and Ahedo observed a low magnetic field region near the plume axis that resulted in plasma detachment while the induced magnetic field didn't produce detachment at the plume edges [10].

Figure 6.2 shows long-time averaged domain pressure, density, and velocity (in the y-direction) for argon at the nozzle offset of 14°. Compared with the 0° case, maximum values of velocity and density remained relatively unchanged, while for pressure the maximum values decreased slightly (Figure 5.8). A slight tilt of low pressure "lobes" in the plume region can be seen from the pressure plot. The pressure gradient pattern appears almost identical to the 0° case. The long-time averaged density plot shows the most distinct effect of nozzle angle, where a rightwards tilt in the low density "lobes" can be seen. The strong density gradient central to the plume shows separation, while the rest of the density gradients are similar to the 0° case. The y-direction velocity plot also shows a rightward tilt most prominently visible in the plume region colored in red.

(a) Pressure in Pa

(b) Density in kg/m^3
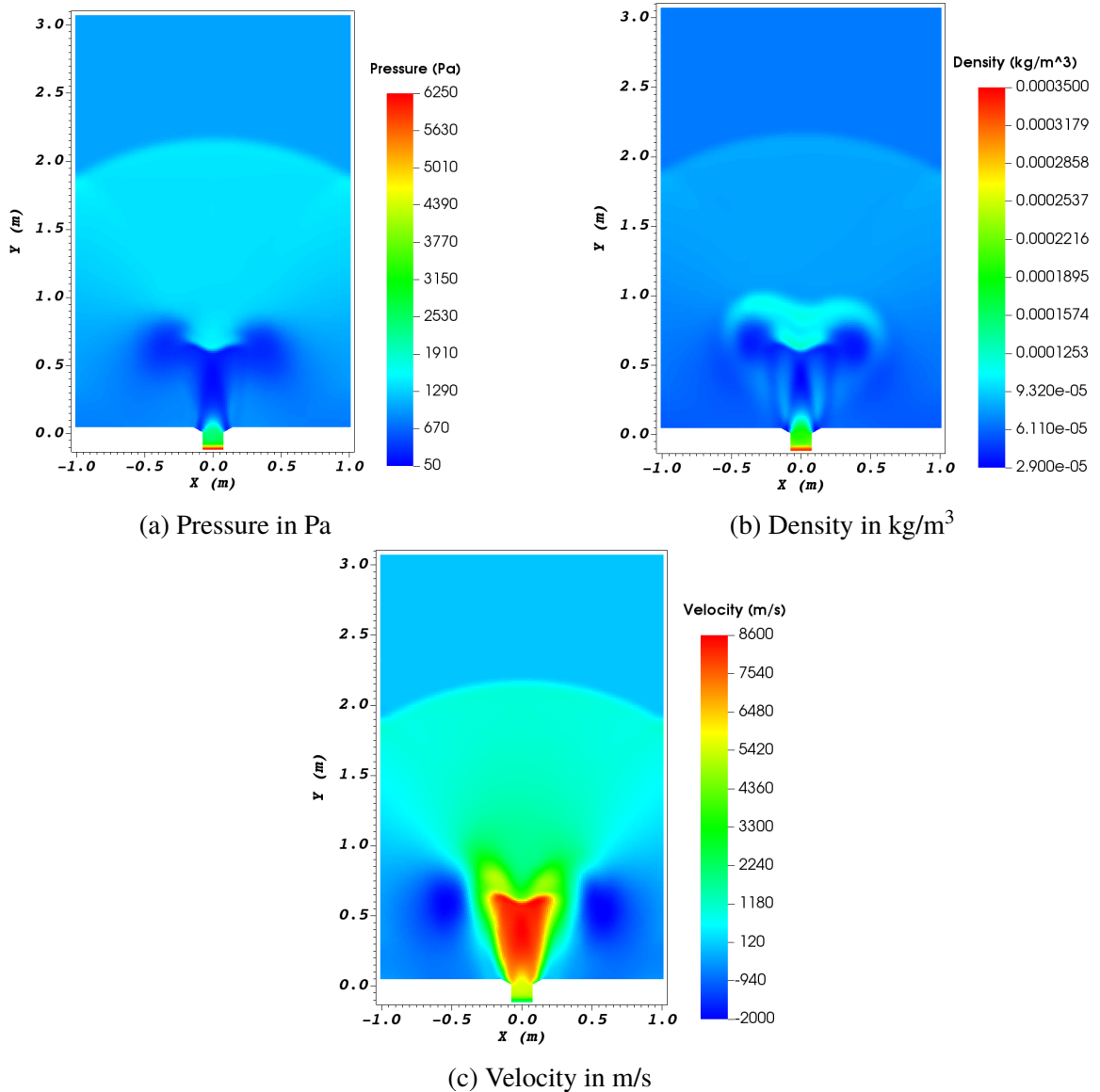
(c) Velocity in m/s

Figure 6.2. Long-time averaged domain pressure, density, and velocity (in the *y*-direction) for argon at a nozzle offset of 14°.

6.2. XENON

Similar to the argon case, Figure 6.3 shows the velocity vectors for xenon at 14° offset angle and 90° phase angle, in comparison with that of 0° offset. Both velocity vector plots look nearly identical. These vectors in showed an average of 0.79° plume offset for xenon. This value was found by averaging all plume vectors with magnitude larger than

over 2,200 m/s in order to find the vectoring angle of the primary plume region excluding far field values. The xenon velocity showed an increase of 1,277m/s through the nozzle at 14°. Only the red vectors at the leading plume edge show the vectoring effect.

(a) Velocity in m/s at 0°   (b) Velocity in m/s at 14°
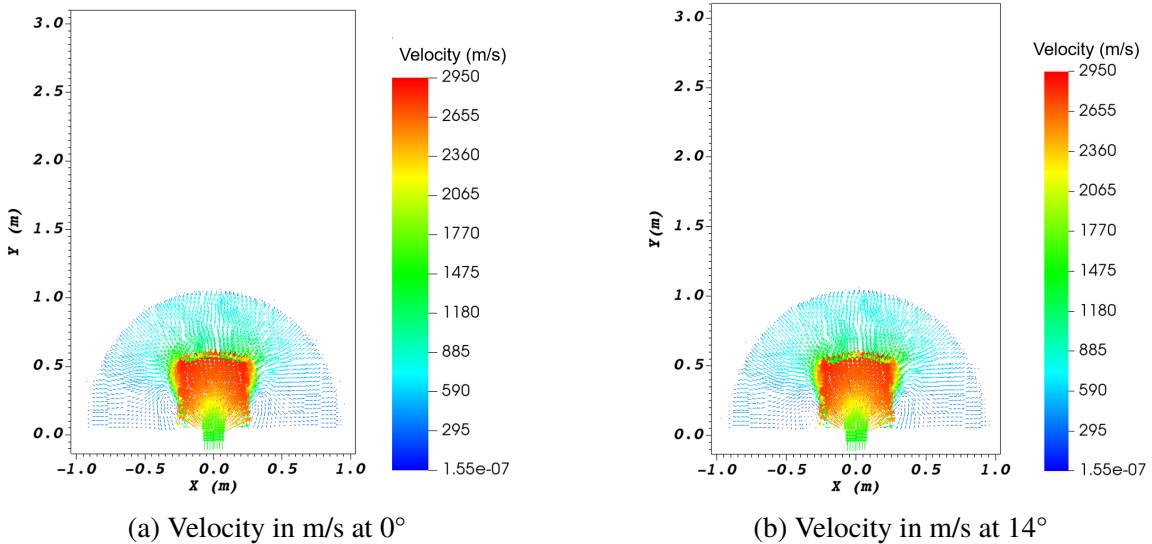
Figure 6.3. Xenon velocity vectors at a time of 4.81111×10^{-4} seconds (90° phase angle) for 0° and 14° of nozzle offset (perpendicular to plasma flow).

Figure 6.4 shows long-time averaged domain pressure, density, and velocity (in the *y*-direction) for xenon at the nozzle offset of 14°. The offset profiles for xenon show no significant change in all three parameters. Maximum values for the three parameters were slightly less than those for the 0° case. The pressure plot shows a flattening of the low pressure region between the plume and nozzle. Asymmetry can be observed within the nozzle where higher values are seen as the plasma approaches the lower end of the coil. The density plot shows a slight rightward bias in the higher density front at the inner plume leading edge (green region). The vectoring effect is better visualized through the *y*-direction velocity where the red plume region protrudes on the right side.

Overall, long-time averaged flow fields show argon has nearly three times the vectoring potential over xenon. Argon also has over four times the velocity increase over xenon. The argon plume is more constrained near the nozzle exit by the magnetic field. The argon also shows a larger area of the plume separating and following the curvature of the

field lines. Arefiev and Breizman, using an ideal MHD analytic solution, determined that inefficiency of detachment was reduced as the nozzle was lengthened [4]. The relatively short nozzle used in this study may lead to less detachment than if the nozzle domain region was extended.

6.3. ARGON USING EXTREME PARAMETER VALUES

In order to explore the plume vectoring limits using extreme parameter values, three additional runs were carried out varying coil amperage, inlet plasma velocity, or both for argon. The coil current was increased to 14,000 A in the first case, the inlet velocity was decreased to 500 m/s in the second, and coil current was increased to 14,000 A and inlet velocity was decreased to 500 m/s in the third.

Figure 6.5 show velocity vectors of these three cases. These three runs resulted in increased plume offset angles of 4.35° when increasing amperage , 5.66° when decreasing velocity, and 8.82° when increasing amperage and decreasing velocity. These values were found by averaging all plume vectors over 6,500 m/s magnitude in order to find the vectoring angle of the primary plume region and exclude far field values. The 14,000 A case shows a widened high velocity plume region in red. The vectoring effect is more prominent but so is the magnetic attachment. In this case, the requisite velocity for detachment was approximately 6,400 m/s determined by the highest values observed within the plume "arms". While the coil amperage was increased by 10,000 A, the coil's accelerative increase was minimal. The plume maximum velocity and vectoring angle increased by only 64 m/s and 2° respectively. The 500 m/s case shows greater promise in enhancing the thruster plume. The magnetic attachment in the plume "arms" was less prominent with the requisite velocity decreasing to approximately 1,800 m/s. Maximum velocity seen in the plume was 7,292 m/s which is an increase of 6,792 m/s over the inlet value. The increase in vectoring angle of approximately 3.3° along with a velocity speedup of 14.6 times makes this a promising avenue for future studies. Increasing coil amperage and lowering inlet

velocity resulted in an increase in vectoring angle of 6.5° and a more focused plume but the lowest peak velocity. It is noted here that larger angles of plume vectoring have been reported in other studies. For instance, Merino and Ahedo demonstrated theoretically a 15° plume vectoring angle within a 3-D magnetic nozzle with three coils can be achieved [15], where the plasma density was about three orders of magnitude less than the values used in this paper. Another study by Morita et al. achieved 20° of plasma flow vectoring using two rectangular coils operated at 3 kA each with a pulsed laser plasma source [28], however the nozzle topology was quite different with no physical inlet wall to confine the flow.

(a) Pressure in Pa

(b) Density in kg/m^3
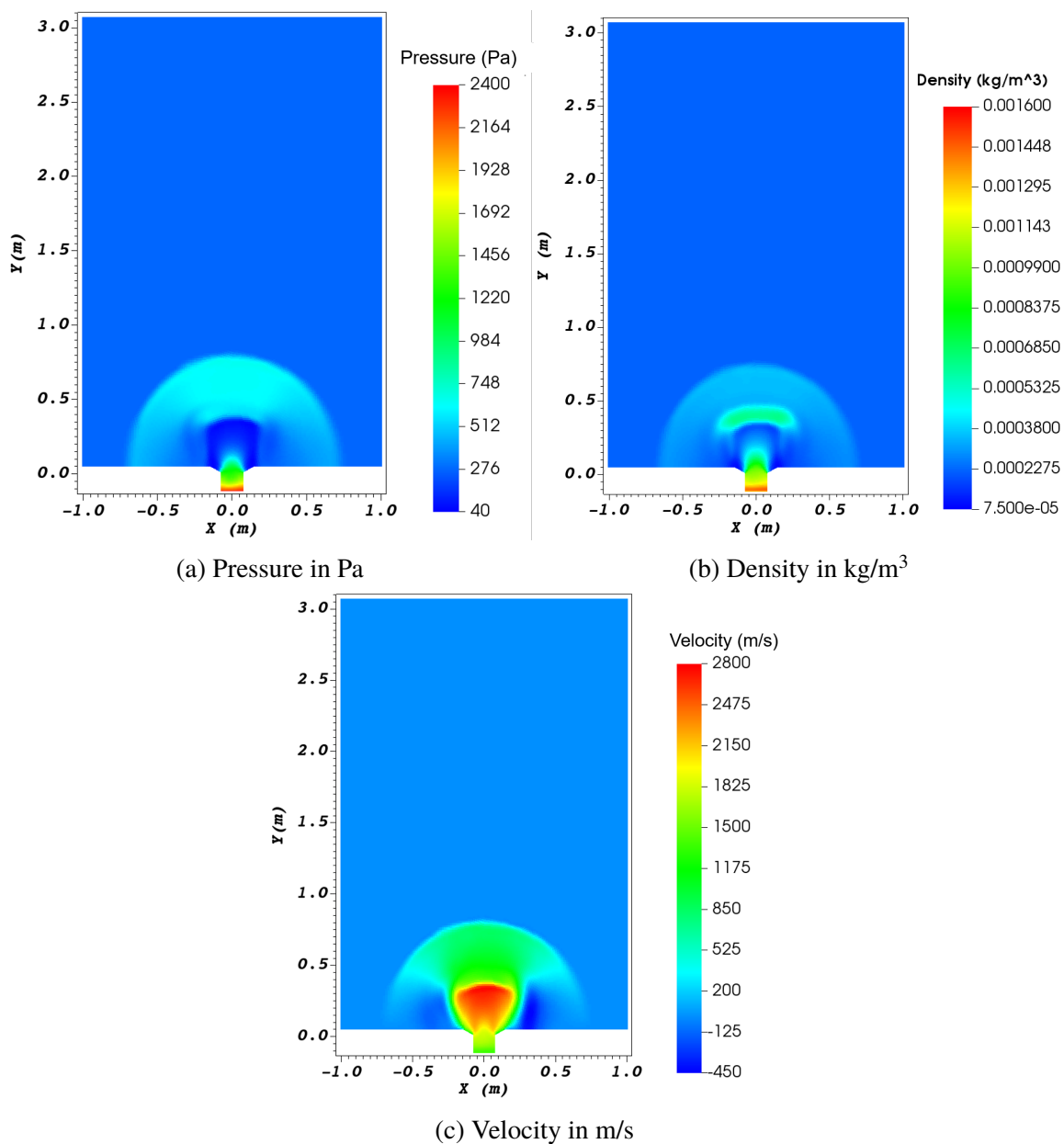
(c) Velocity in m/s

Figure 6.4. Long-time averaged domain pressure, density, and velocity (in the *y*-direction) for xenon at a nozzle offset of 14°.

(a) 14,000 A coil current

(b) 500 m/s inlet velocity

(c) 14,000 A coil current and 500 m/s inlet velocity
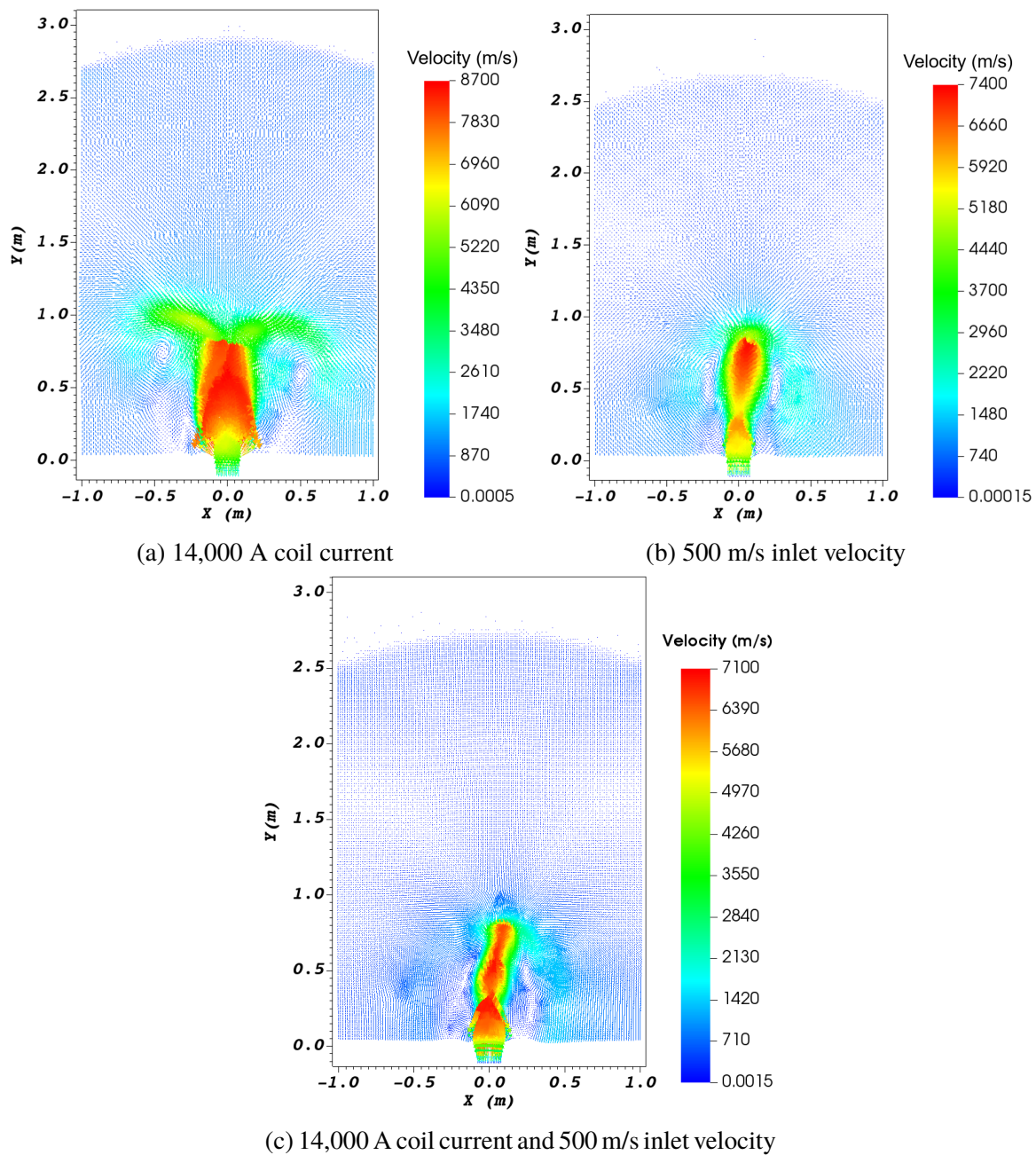
Figure 6.5. Velocity vectors in m/s for argon at 14° nozzle offset with extreme parameter values.

7. SUMMARY AND CONCLUSION

In summary, 2-D numerical simulations were carried out to quantify effects of magnetic nozzles for a representative PIP source. Simulations were verified and validated through a mesh convergence study as well as comparison with available experimental data. Periodicity of solutions was achieved when analyzing phase-angle and long-time averaged flow field quantities. Both argon and xenon plasmas were investigated. Pressure values at different phase angles for a single pulse showed little variation in the plume and slight variation at the inlet. Long-time averaged flow fields showed little variation from the phase angle values due to the subtle effect the periodic inflow has after periodicity has been reached. The effects of a magnetic nozzle offset up to 14° show a maximum plume angle of 2.32° for argon and 0.79° for xenon. Argon shows a stronger susceptibility to magnetic steering than the heavier and slower xenon. Argon demonstrated three times the vectoring angle and four times the velocity increase compared to xenon. Improved angles were achieved through a significant yet unrealistic increase in coil amperage and decrease in inlet velocity. The effect of increased coil amperage on thruster performance showed a marginal velocity increase and approximately 2° additional vectoring at the cost of additional losses through greater magnetic attachment. The effect of decreased inlet velocity demonstrated an increase in plume vectoring angle and greater plume acceleration. Combining these large parameter changes resulted in the lowest magnetic attachment and highest vectoring angle at the cost of plume acceleration. Argon shows a stronger susceptibility to magnetic steering than the heavier and slower xenon. Argon demonstrated three times the vectoring angle and four times the velocity increase compared to xenon.

Based on these findings, it can be concluded that the application of a magnetic nozzle for steering the plume of a PIP source with the configuration and plume parameters presented here is not feasible for state-of-the-art in-space propulsion due to the large current required to achieve a useful offset angle. Further investigations are necessary to find a configuration that will allow for beneficial plume vectoring.

APPENDIX

ADDITIONAL LONG-TIME AVERAGED FLOW FIELDS

(a) Pressure in Pa

(b) Density in kg/m^3
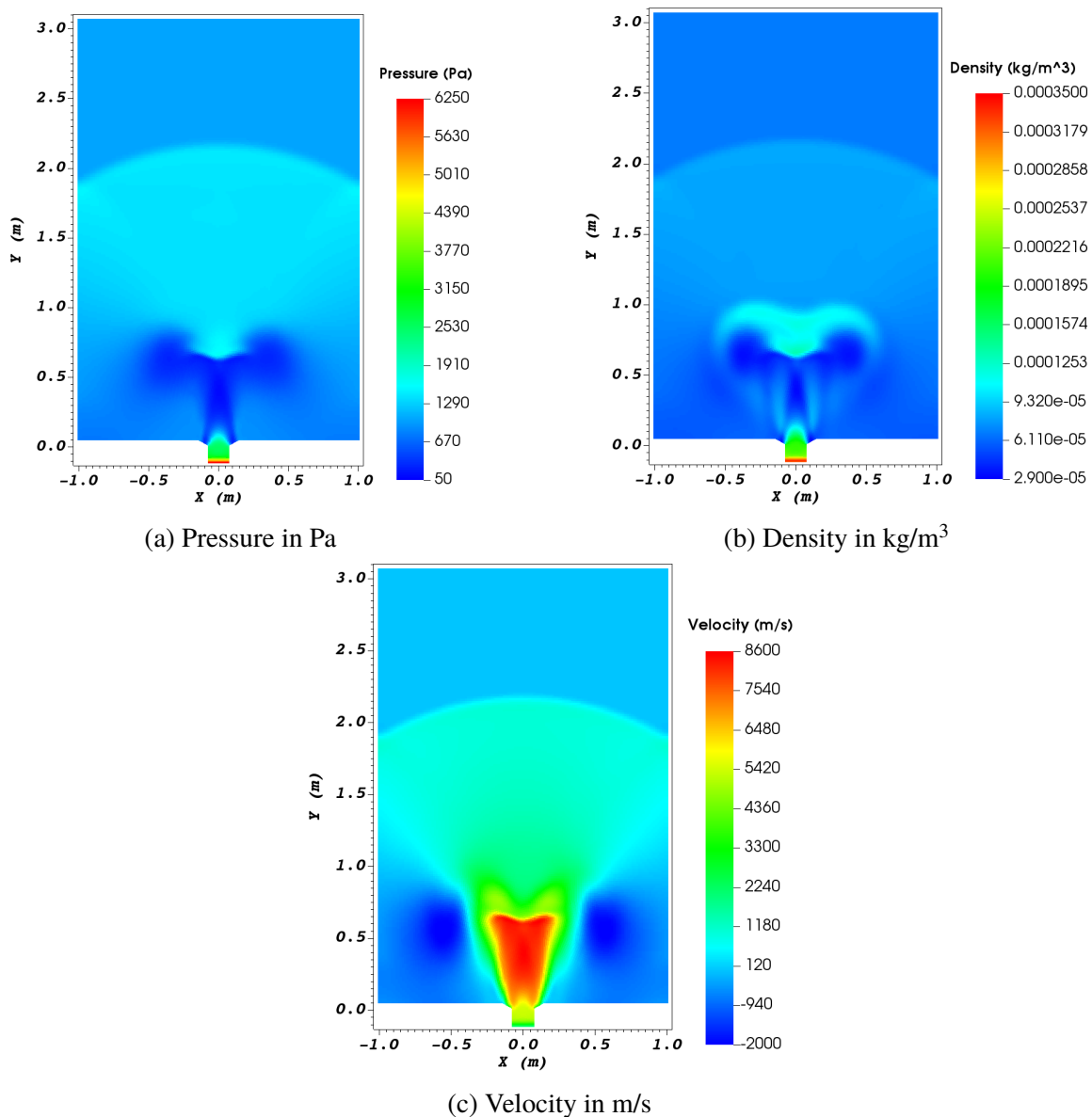
(c) Velocity in m/s

Figure 1. Long-time averaged domain pressure, density, and velocity (in the *y*-direction) for argon at a nozzle offset of 2°.

(a) Pressure in Pa

(b) Density in kg/m^3
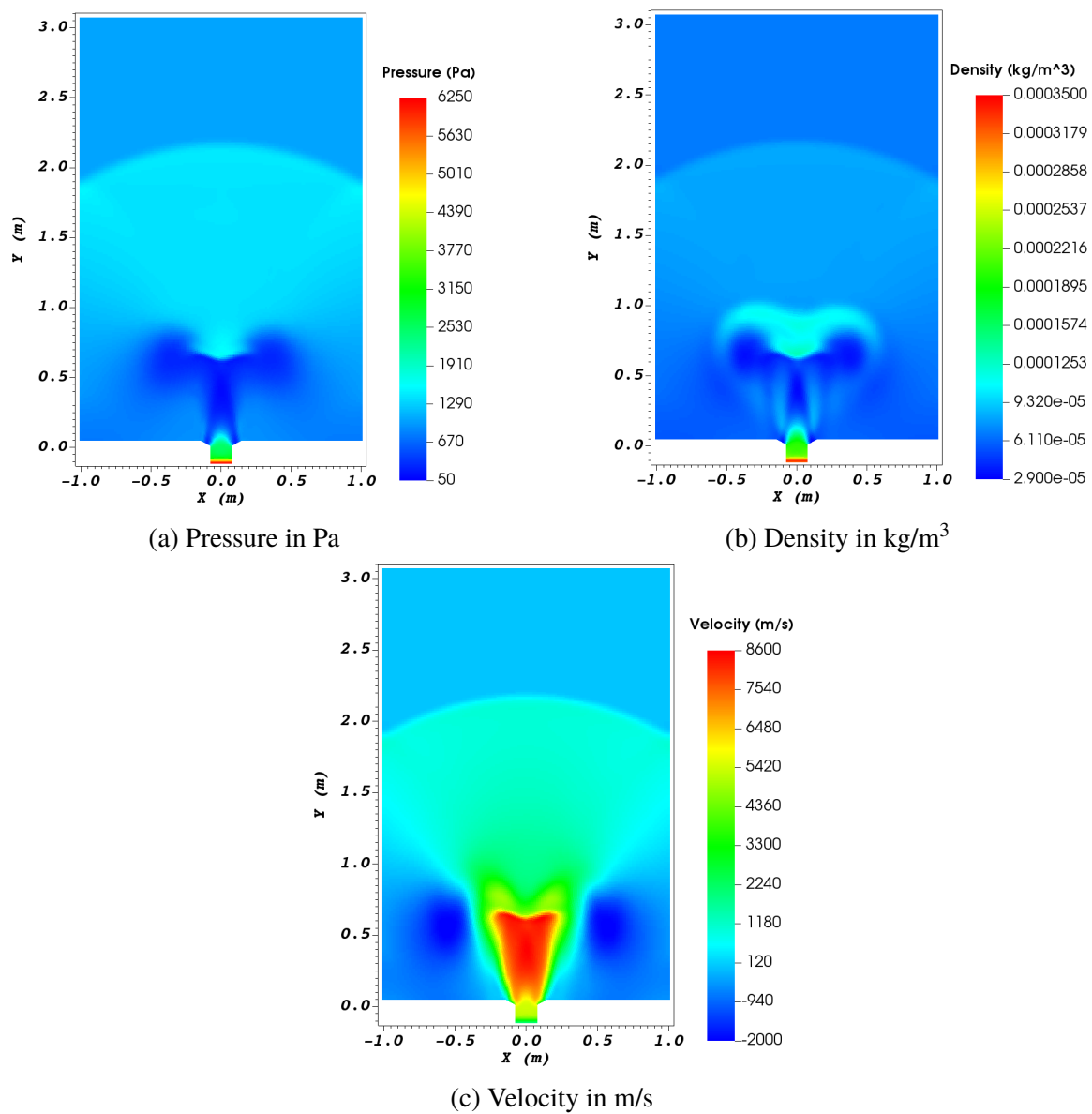
(c) Velocity in m/s

Figure 2. Long-time averaged domain pressure, density, and velocity (in the *y*-direction) for argon at a nozzle offset of 4°.

(a) Pressure in Pa

(b) Density in kg/m^3
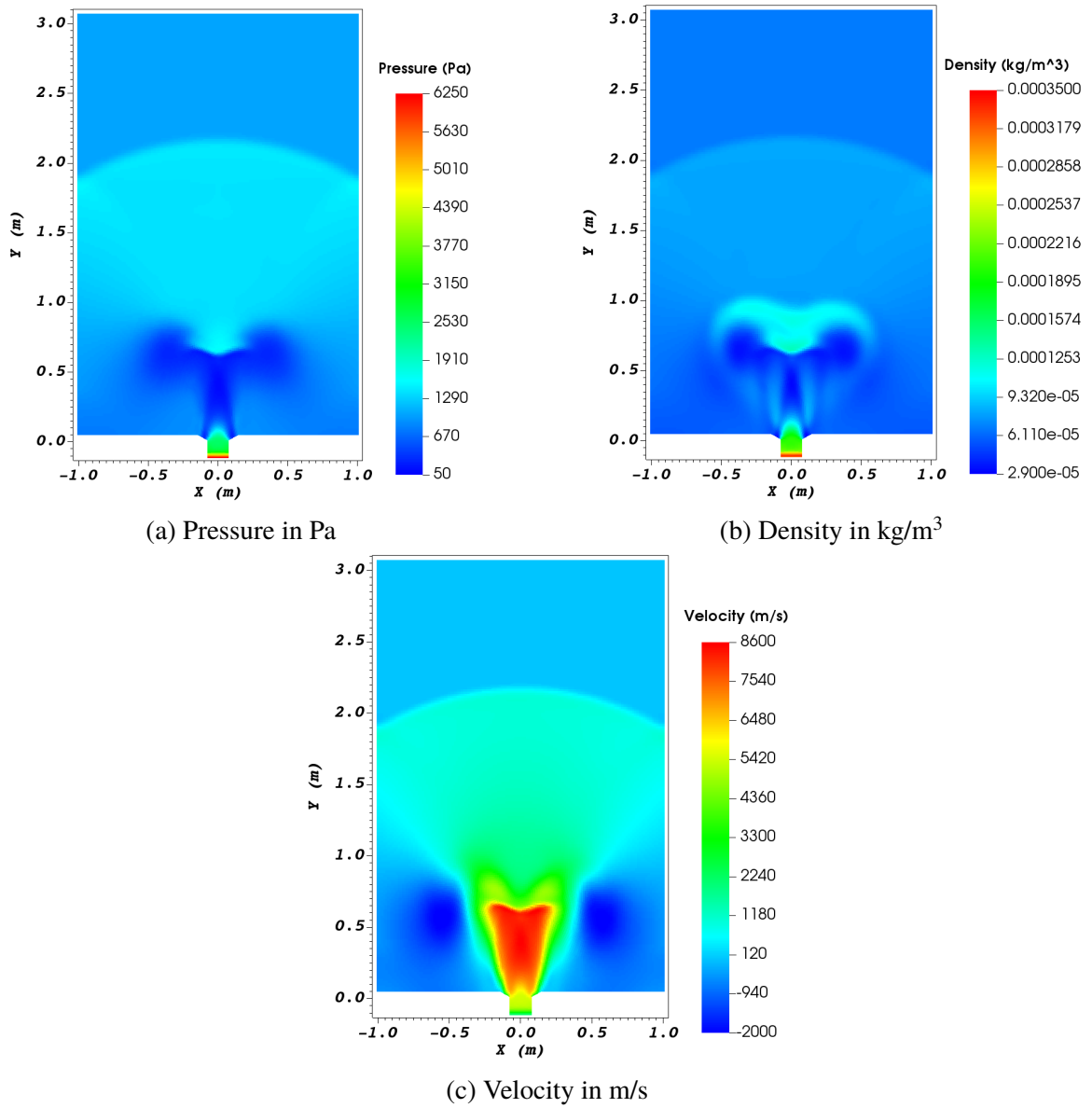
(c) Velocity in m/s

Figure 3. Long-time averaged domain pressure, density, and velocity (in the *y*-direction) for argon at a nozzle offset of 6°.

(a) Pressure in Pa

(b) Density in kg/m^3
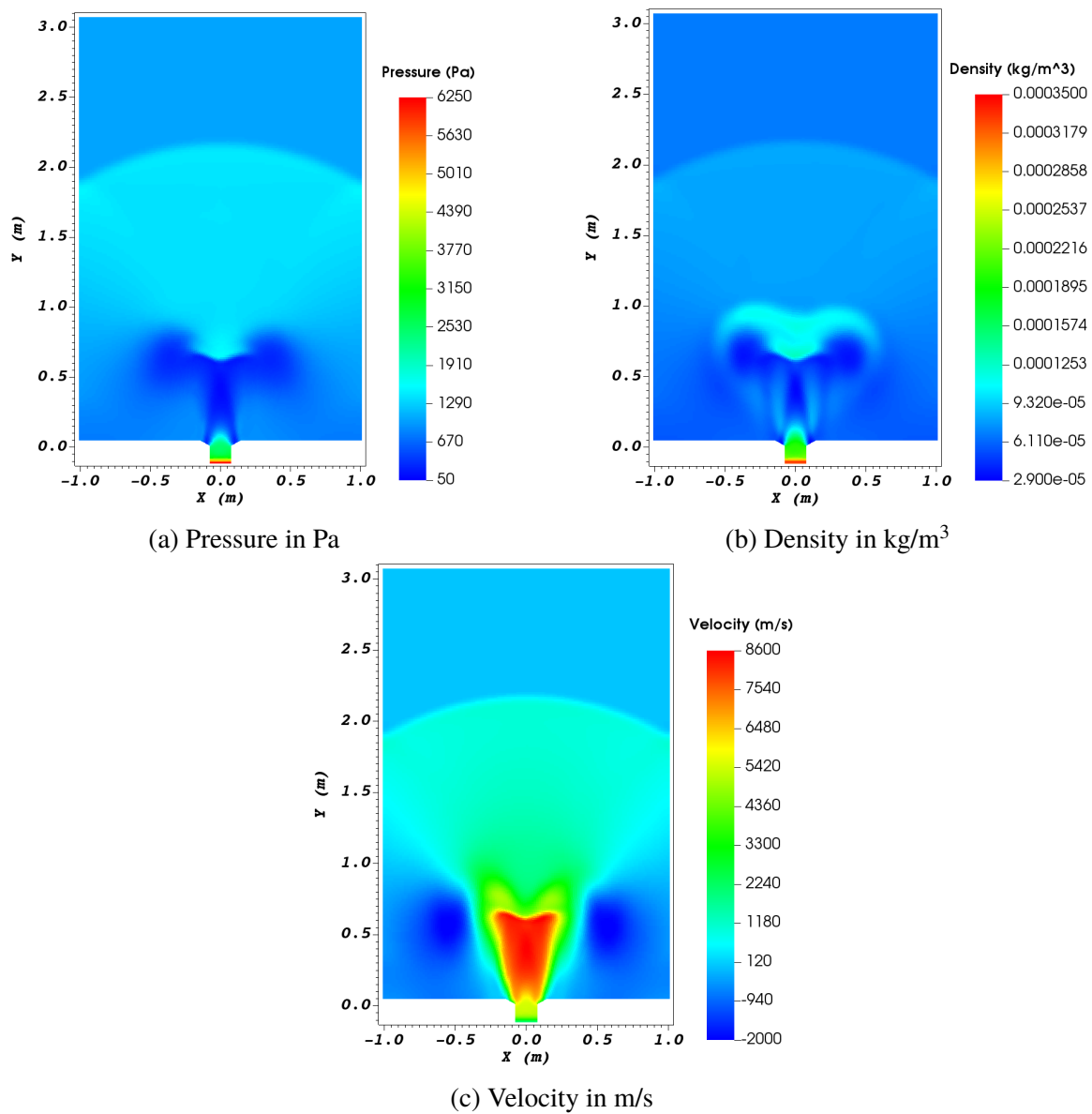
(c) Velocity in m/s

Figure 4. Long-time averaged domain pressure, density, and velocity (in the *y*-direction) for argon at a nozzle offset of 8°.

(a) Pressure in Pa

(b) Density in kg/m^3
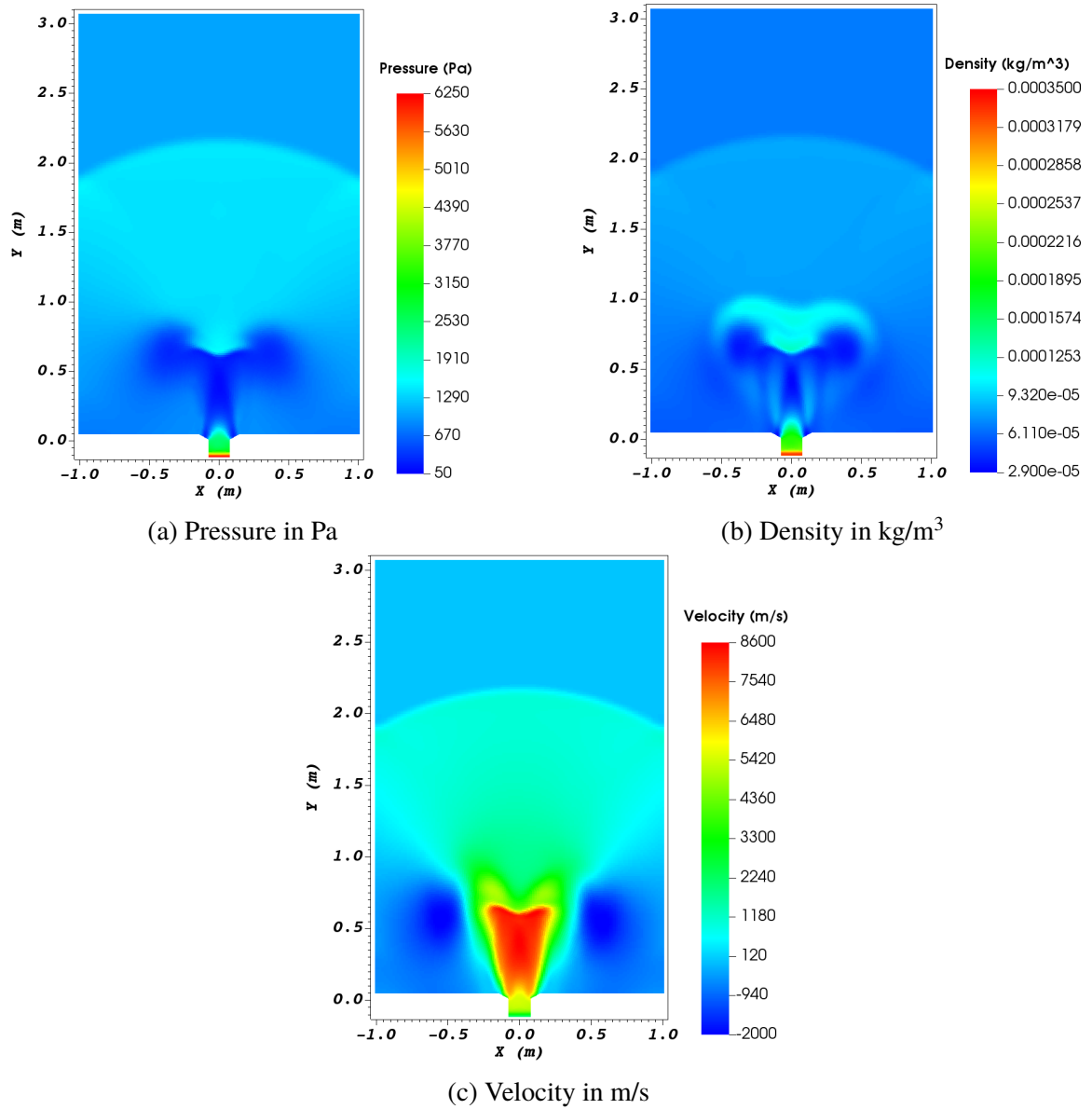
(c) Velocity in m/s

Figure 5. Long-time averaged domain pressure, density, and velocity (in the *y*-direction) for argon at a nozzle offset of 10°.

(a) Pressure in Pa

(b) Density in kg/m^3
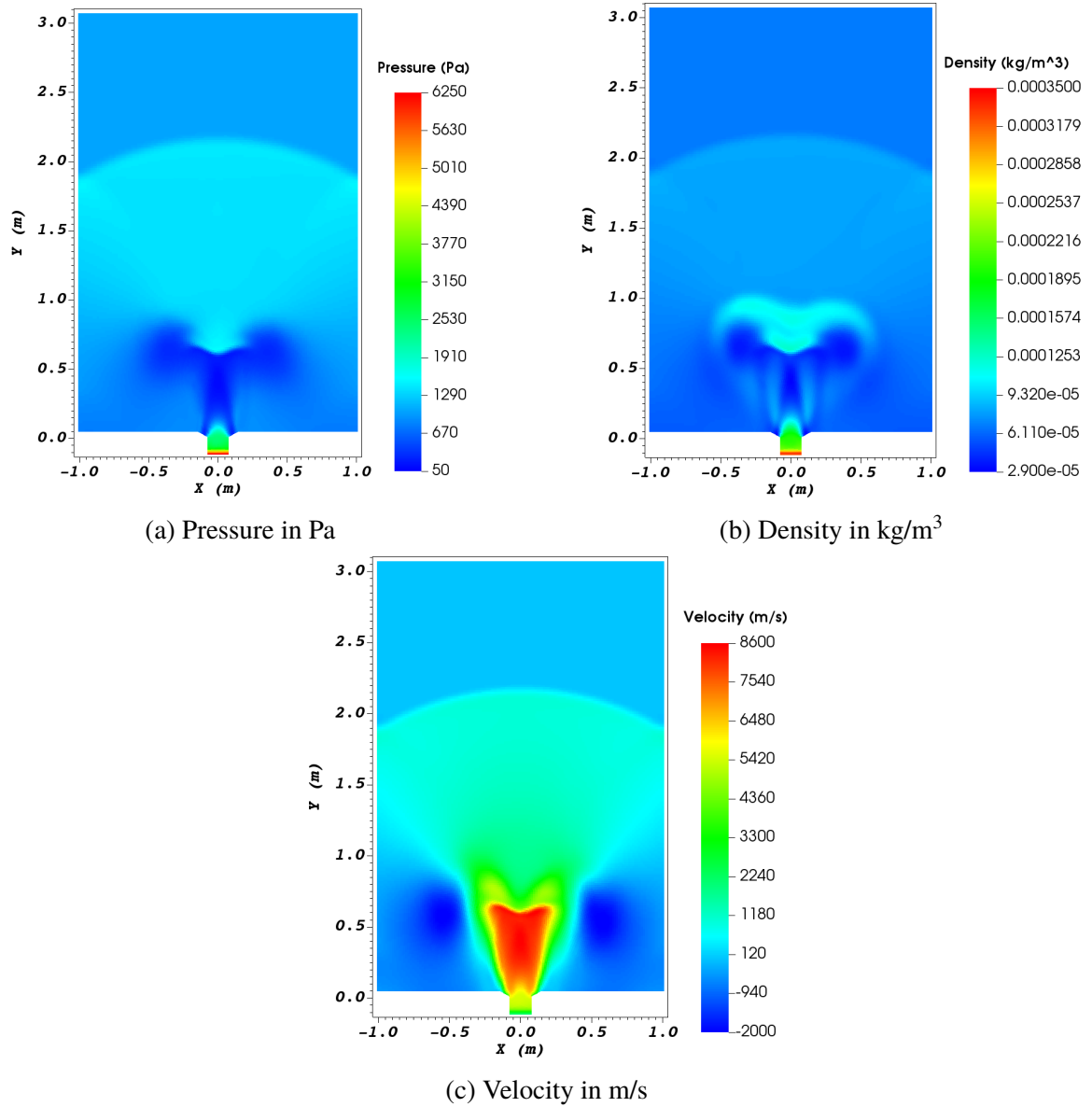
(c) Velocity in m/s

Figure 6. Long-time averaged domain pressure, density, and velocity (in the *y*-direction) for argon at a nozzle offset of 12°.

(a) Pressure in Pa

(b) Density in kg/m^3
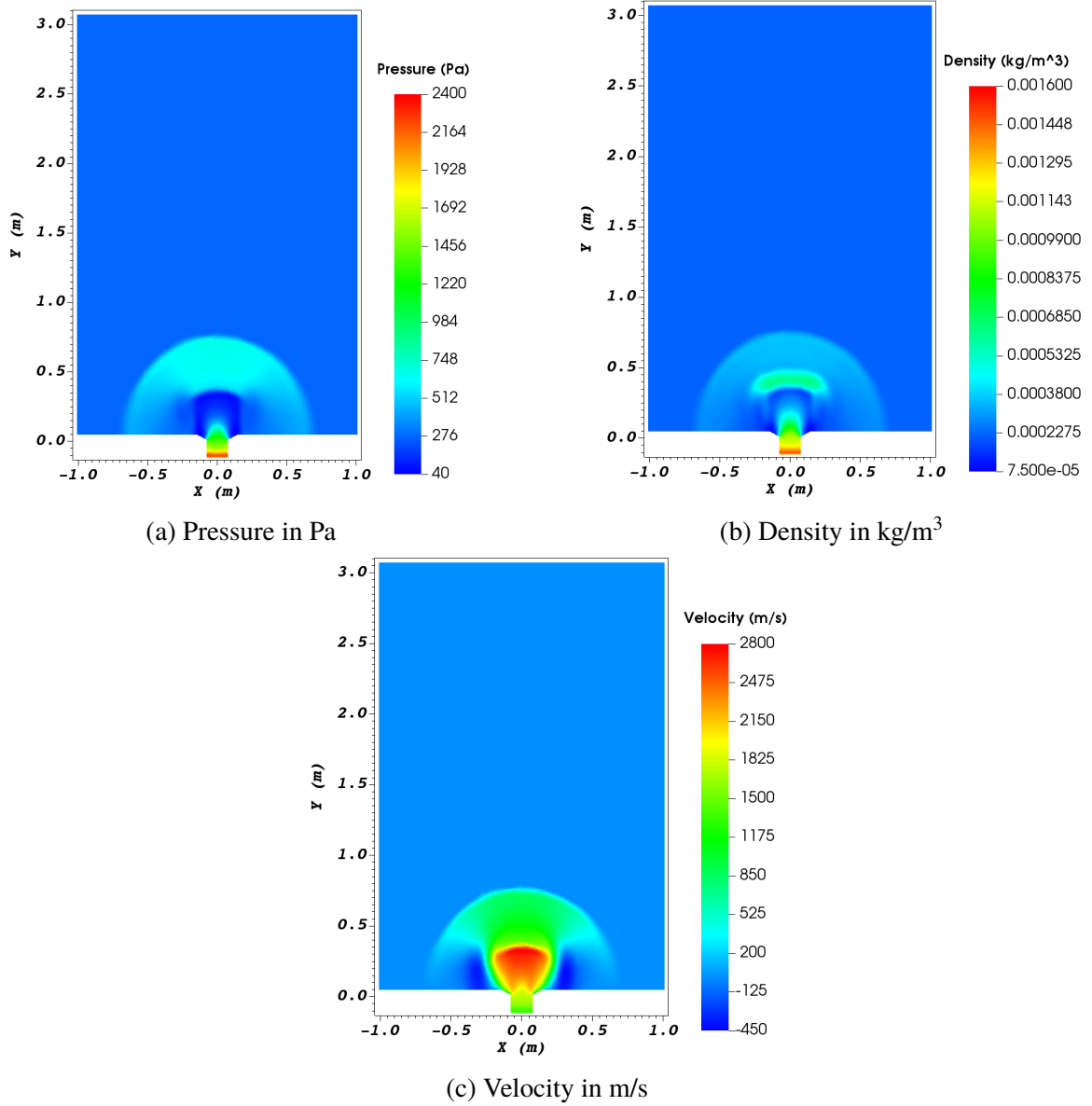
(c) Velocity in m/s

Figure 7. Long-time averaged domain pressure, density, and velocity (in the y-direction) for xenon at a nozzle offset of 2°.

(a) Pressure in Pa

(b) Density in kg/m^3
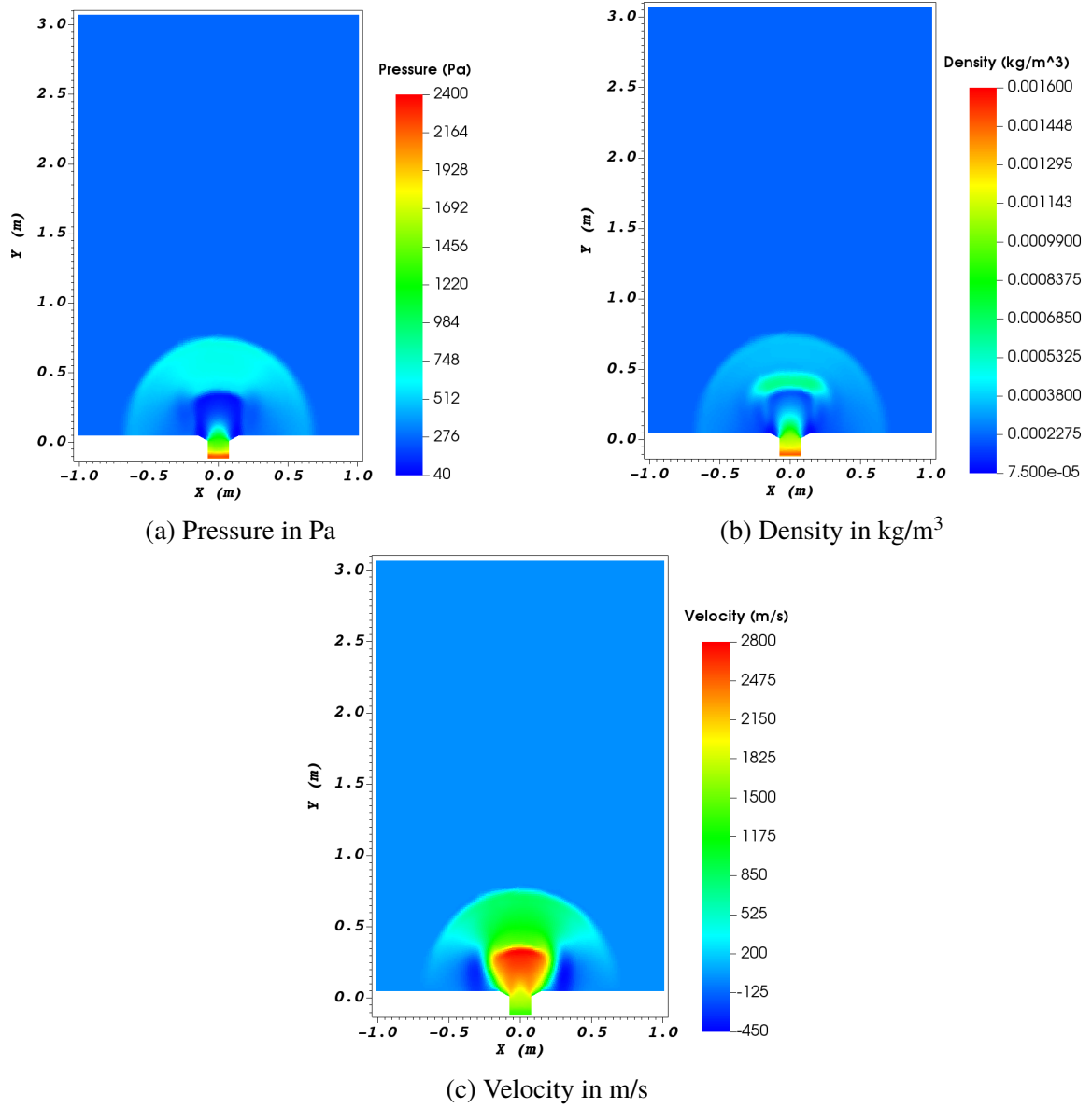
(c) Velocity in m/s

Figure 8. Long-time averaged domain pressure, density, and velocity (in the *y*-direction) for xenon at a nozzle offset of 4°.

(a) Pressure in Pa

(b) Density in kg/m^3
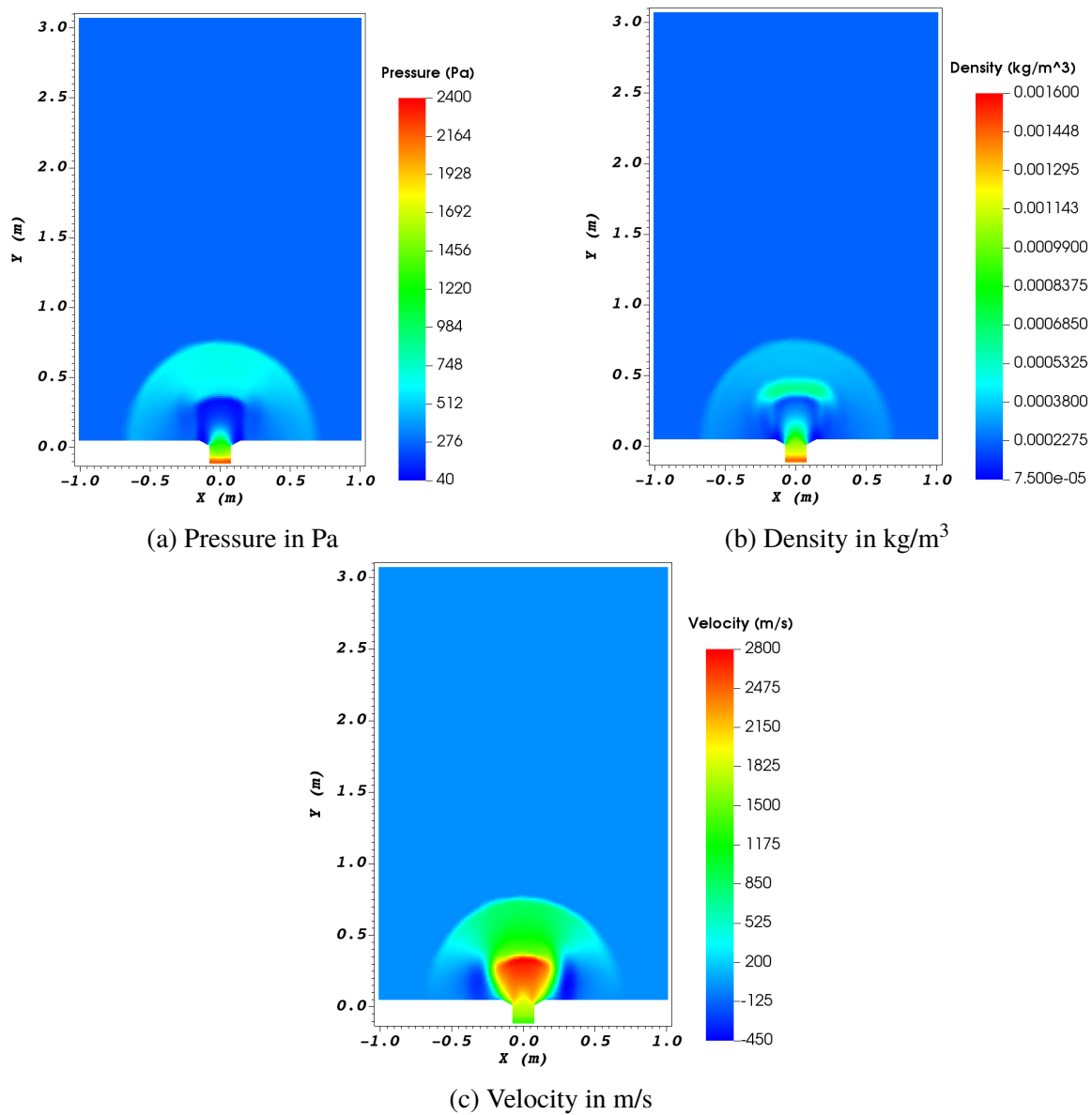
(c) Velocity in m/s

Figure 9. Long-time averaged domain pressure, density, and velocity (in the *y*-direction) for xenon at a nozzle offset of 6°.

(a) Pressure in Pa

(b) Density in kg/m^3
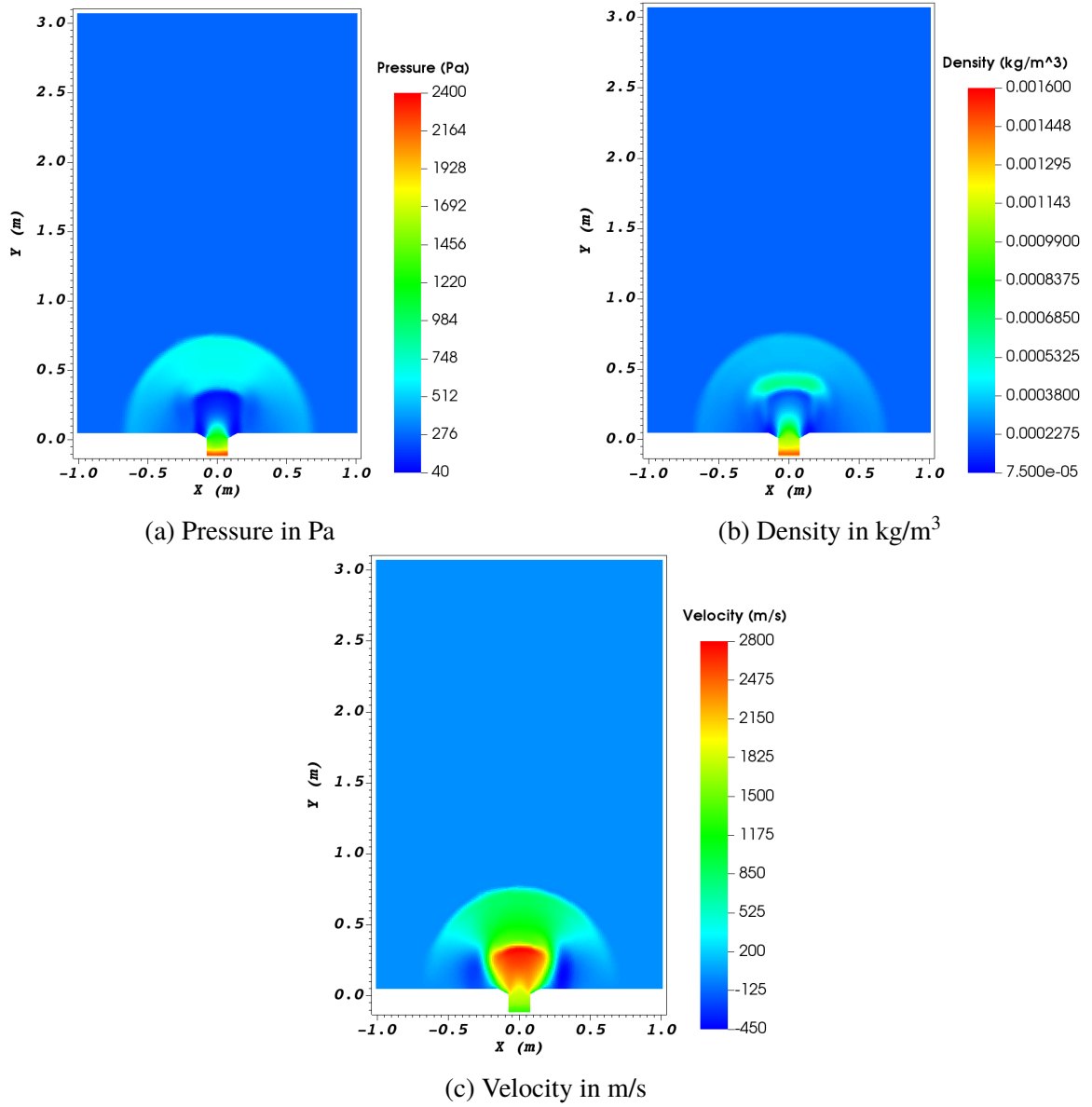
(c) Velocity in m/s

Figure 10. Long-time averaged domain pressure, density, and velocity (in the *y*-direction) for xenon at a nozzle offset of 8°.

(a) Pressure in Pa

(b) Density in kg/m^3
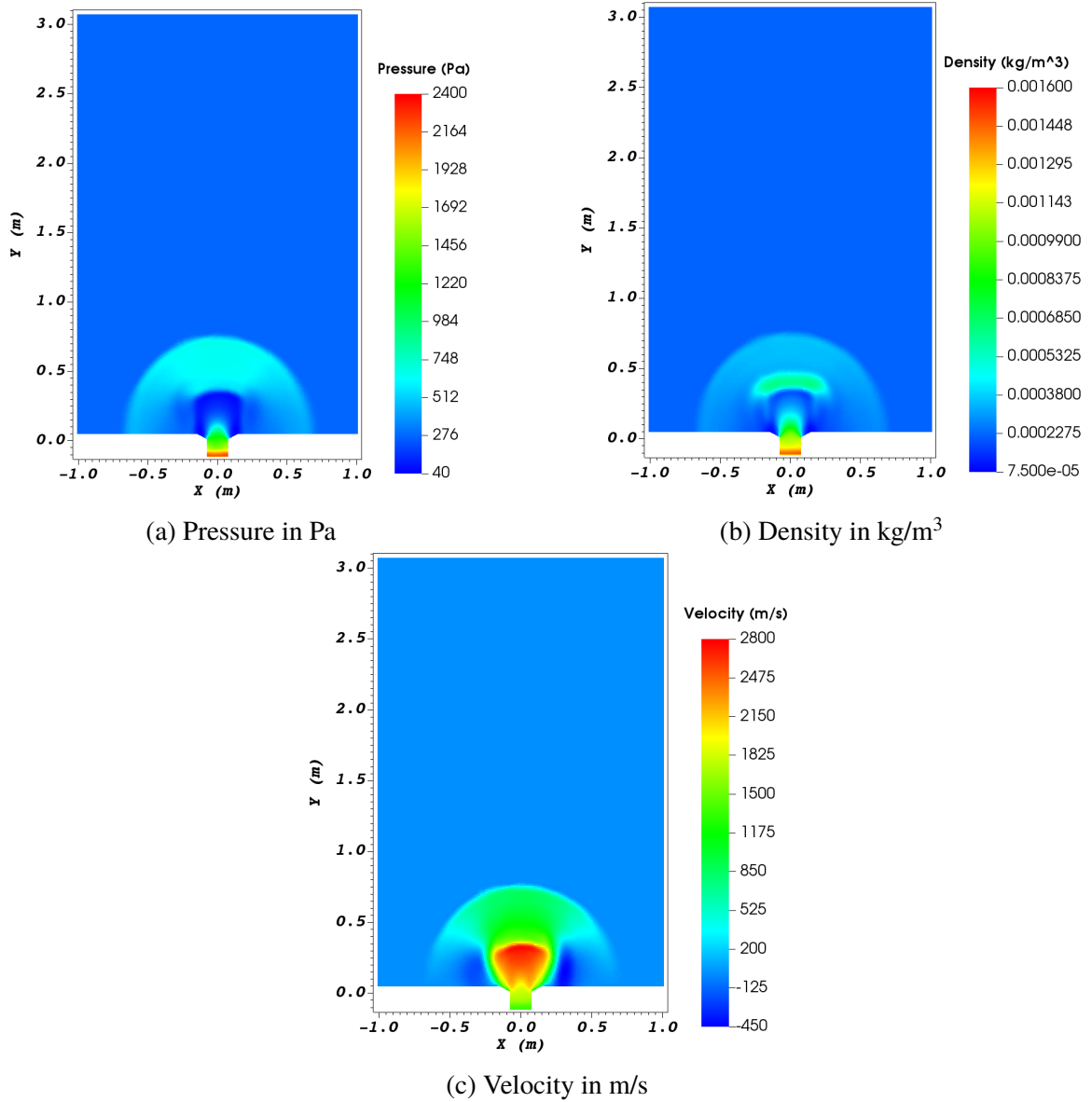
(c) Velocity in m/s

Figure 11. Long-time averaged domain pressure, density, and velocity (in the *y*-direction) for xenon at a nozzle offset of 10°.

(a) Pressure in Pa

(b) Density in kg/m³
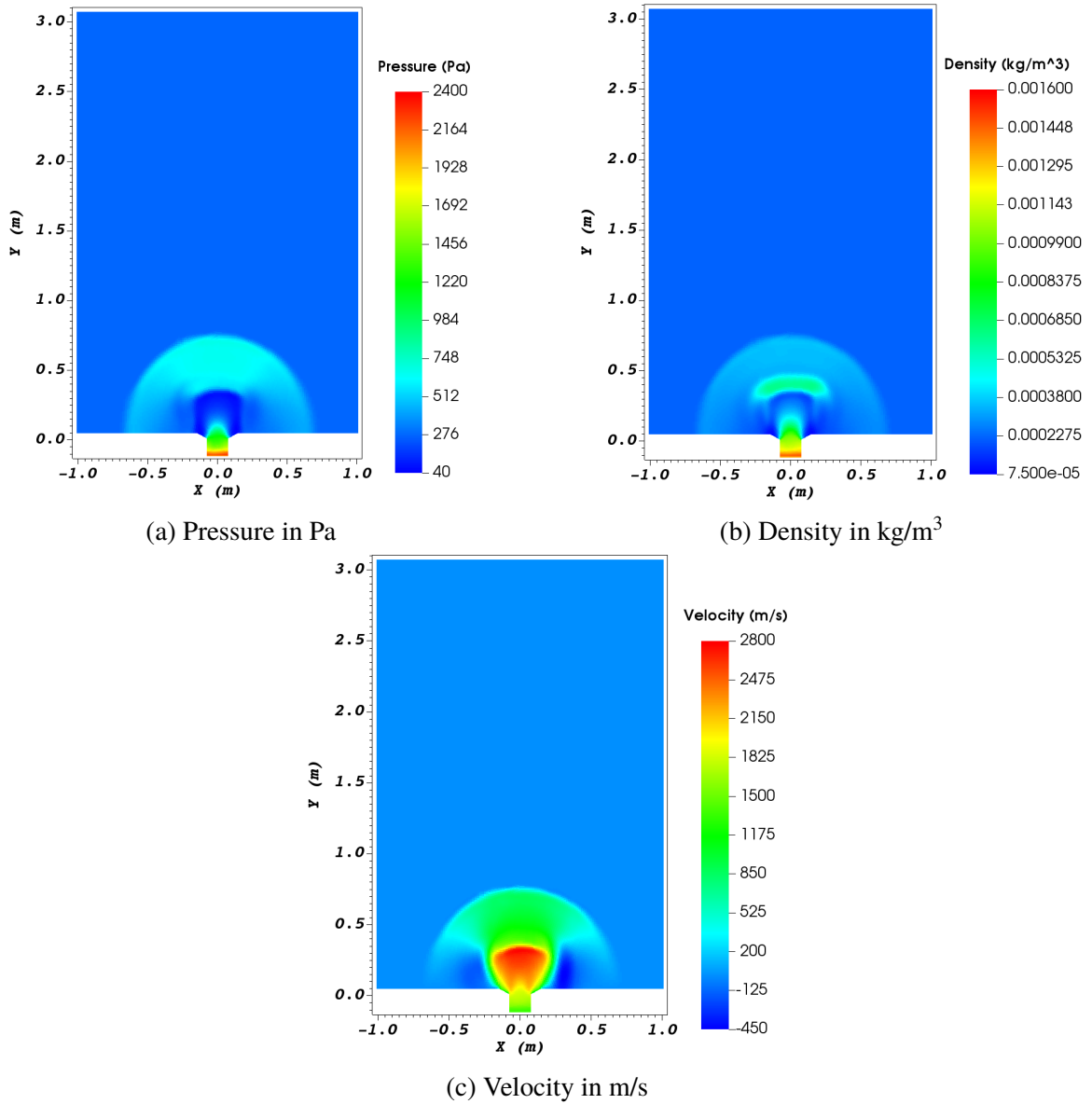
(c) Velocity in m/s

Figure 12. Long-time averaged domain pressure, density, and velocity (in the *y*-direction) for xenon at a nozzle offset of 12°.

REFERENCES

[1] K. A. Polzin. Comprehensive Review of Planar Pulsed Inductive Plasma Thruster Research and Technology. *Journal of Propulsion and Power*, 27(3):513–531, May 2011. doi: 10.2514/1.b34188.

[2] R. Pahl and J. Rovey. Energy Analysis of a Pulsed Inductive Plasma Through Circuit Simulation. *IEEE Transactions on Plasma Science*, 42(10):3411–3418, September 2014. doi: 10.1109/TPS.2014.2355717.

[3] J. Loverich and A. Hakim. Two-Dimensional Modeling of Ideal Merging Plasma Jets. *Journal of Fusion Energy*, 29(6):532–539, August 2010. doi: 10.1007/s10894-010-9 321-z.

[4] A. V. Arefiev and B. N. Breizman. Magnetohydrodynamic scenario of plasma detachment in a magnetic nozzle. *Physics of Plasmas*, 12(4):043504, April 2005. doi: 10.1063/1.1875632.

[5] B. N. Breizman, M. R. Tushentsov, and A. V. Arefiev. Magnetic nozzle and plasma detachment model for a steady-state flow. *Physics of Plasmas*, 15(5):057103, May 2008. doi: 10.1063/1.2903844.

[6] E. Ahedo and M. Merino. Two-Dimensional Plasma Acceleration in a Divergent Magnetic Nozzle. In *45th AIAA/ASME/SAE/ASEE Joint Propulsion Conference & Exhibit*. American Institute of Aeronautics and Astronautics, August 2009. doi: 10.2 514/6.2009-5361.

[7] E. Ahedo and M. Merino. Two-dimensional supersonic plasma acceleration in a magnetic nozzle. *Physics of Plasmas*, 17(7):073501, July 2010. doi: 10.1063/1.3442 736.

[8] M. Merino, F. Cichocki, and E. Ahedo. A collisionless plasma thruster plume expansion model. *Plasma Sources Science and Technology*, 24(3):035006, April 2015. doi: 10.1088/0963-0252/24/3/035006.

[9] M. Merino and E. Ahedo. Simulation of Plasma Flows in Divergent Magnetic Nozzles. *IEEE Transactions on Plasma Science*, 39(11):2938–2939, November 2011. doi: 10.1109/tps.2011.2158325.

[10] M. Merino and E. Ahedo. Plasma detachment mechanisms in a magnetic nozzle. In *47th AIAA/ASME/SAE/ASEE Joint Propulsion Conference & Exhibit*. American Institute of Aeronautics and Astronautics, July 2011. doi: 10.2514/6.2011-5999.

[11] E. Ahedo and M. Merino. On plasma detachment in propulsive magnetic nozzles. *Physics of Plasmas*, 18(5):053504, May 2011. doi: 10.1063/1.3589268.

[12] M. Merino and E. Ahedo. Influence of Electron and Ion Thermodynamics on the Magnetic Nozzle Plasma Expansion. *IEEE Transactions on Plasma Science*, 43(1): 244–251, January 2015. doi: 10.1109/tps.2014.2316020.

[13] M. Merino and E. Ahedo. Effect of the plasma-induced magnetic field on a magnetic nozzle. *Plasma Sources Science and Technology*, 25(4):045012, June 2016. doi: 10.1088/0963-0252/25/4/045012.

[14] M. Merino and E. Ahedo. Fully magnetized plasma flow in a magnetic nozzle. *Physics of Plasmas*, 23(2):023506, February 2016. doi: 10.1063/1.4941975.

[15] M. Merino and E. Ahedo. Contactless steering of a plasma jet with a 3D magnetic nozzle. *Plasma Sources Science and Technology*, 26(9):095001, August 2017. doi: 10.1088/1361-6595/aa8061.

[16] P. Jiménez, M. Merino, and E. Ahedo. Preliminary investigation of the electromagnetic fields in the far plume of a Helicon Plasma Thruster. In *Student Paper Contest 2020*. IEEE, 2020.

[17] Y. Hu, Z. Huang, Y. Cao, and Q. Sun. Kinetic insights into thrust generation and electron transport in a magnetic nozzle. *Plasma Sources Science and Technology*, 30 (7):075006, July 2021. doi: 10.1088/1361-6595/ac0a48.

[18] J. Zhou, G. Sanchez-Arriaga, and E. Ahedo. Time-dependent expansion of a weakly-collisional plasma beam in a paraxial magnetic nozzle. *Plasma Sources Science and Technology*, March 2021. doi: 10.1088/1361-6595/abeff3.

[19] R. Pahl, W. Meeks, and J. Rovey. Magnetic Field Mapping of a Field Reversed Configuration Test Article. In *47th AIAA/ASME/SAE/ASEE Joint Propulsion Conference & Exhibit*. American Institute of Aeronautics and Astronautics, July 2011. doi: 10.2514/6.2011-5656.

[20] R. Pahl and J. Rovey. Pre-Ionization Plasma in an FRC Test Article. In *50th AIAA Aerospace Sciences Meeting including the New Horizons Forum and Aerospace Exposition*, AIAA 2012-0194, Nashville, Tennessee, January 2012. American Institute of Aeronautics and Astronautics. doi: 10.2514/6.2012-194.

[21] W. C. Meeks and J. L. Rovey. Time-resolved temperature in an argon theta-pinch by line ratio methods. In *2014 IEEE 41st International Conference on Plasma Sciences (ICOPS) held with 2014 IEEE International Conference on High-Power Particle Beams (BEAMS)*. IEEE, May 2014. doi: 10.1109/plasma.2014.7012731.

[22] W. C. Meeks and J. L. Rovey. Optical Emission Spectroscopy of Plasma Formation in a Xenon Theta-Pinch. *IEEE Transactions on Plasma Science*, 42(5):1385–1392, May 2014. doi: 10.1109/tps.2014.2316453.

[23] W. Meeks and J. Rovey. Numerical and experimental efforts to explain delayed gas breakdown in 0-pinch devices with bias magnetic field. In *48th AIAA/ASME/SAE/ASEE Joint Propulsion Conference & Exhibit*. American Institute of Aeronautics and Astronautics, July 2012. doi: 10.2514/6.2012-3929.

[24] W. C. Meeks and J. L. Rovey. Argon and Xenon Pulsed Theta-Pinch Plasma via Optical Emission Spectroscopy. In *33rd International Electric Propulsion Conference*, IEPC-2013-378, Washington, DC, George Washington University, October 2013.

[25] R. A. Pahl and J. L. Rovey. Effects of DC Preionization Voltage and Radial Location on Pulsed Inductive Plasma Formation. *IEEE Transactions on Plasma Science*, 43 (11):3883–3888, November 2015. doi: 10.1109/tps.2015.2484319.

[26] C. A. Deline, R. D. Bengtson, B. N. Breizman, M. R. Tushentsov, J. E. Jones, D. G. Chavers, C. C. Dobson, and B. M. Schuettpelz. Plume detachment from a magnetic nozzle. *Physics of Plasmas*, 16(3):033502, March 2009. doi: 10.1063/1.3080206.

[27] B. W. Longmier, E. A. Bering, M. D. Carter, L. D. Cassady, W. J. Chancery, F. R. Chang Díaz, T. W. Glover, N. Hershkowitz, A. V. Ilin, G. E. McCaskill, C. S. Olsen, and J. P. Squire. Ambipolar ion acceleration in an expanding magnetic nozzle. *Plasma Sources Science and Technology*, 20(1):015007, January 2011. doi: 10.1088/0963-0 252/20/1/015007.

[28] T. Morita, M. Edamoto, S. Miura, A. Sunahara, N. Saito, I. Itadani, T. Kojima, Y. Mori, T. Johzaki, Y. Kajimura, S. Fujioka, A. Yogo, H. Nishimura, H. Nakashima, and N. Yamamoto. Control of unsteady laser-produced plasma-flow with a multiple-coil magnetic nozzle. *Scientific Reports*, 7(1), August 2017. doi: 10.1038/s41598-0 17-09273-3.

[29] Tech-X Corporation. *USim Reference Manual*, 2018. URL `https://www.txcorp .com/images/docs/usim/latest/reference_manual/USimReferenceManua l.html`. [retrieved 20 May 2020].

[30] S. Lee. Radius Ratios of Argon Pinches. *Australian Journal of Physics*, 36(6):891, 1983. doi: 10.1071/ph830891.

[31] S. Jung, V. Surla, T. Gray, D. Andruczyk, and D. Ruzic. Characterization of a theta-pinch plasma using triple probe diagnostic. *Journal of Nuclear Materials*, 415(1): S993–S995, August 2011. doi: 10.1016/j.jnucmat.2011.01.046.

[32] T. A. Marks, I. G. Mikellides, A. Lopez Ortega, and B. Jorns. Hall2De Simulations of a Magnetic Nozzle. In *AIAA Propulsion and Energy 2020 Forum*. American Institute of Aeronautics and Astronautics, August 2020. doi: 10.2514/6.2020-3642.

[33] R. A. Pahl. *Energy deposition into heavy gas plasma via pulsed inductivetheta-pinch*. PhD thesis, Missouri University of Science and Technology, 2014.

[34] W. C. Meeks. *Pulsed inductive plasma studies by spectroscopy and internal probe methods*. phdthesis, Missouri University of Science and Technology, Rolla, MO, 2015.

[35] J. D. Burch, D. Han, and S. N. Averkin. Numerical investigations of 2-D planar magnetic nozzle effects on pulsed plasma plumes. *The Aeronautical Journal*, 126 (1299):793–812, November 2021. doi: 10.1017/aer.2021.100.

[36] J. Nuez, M. Merino, and E. Ahedo. Fluid-kinetic propulsive magnetic nozzle model in thefully magnetized limit. In *36th International Electric Propulsion Conference*, IEPC-2019-254, University of Vienna, Austria, September 2019.

[37] E. Ahedo and J. Navarro-Cavallé. Helicon thruster plasma modeling: Two-dimensional fluid-dynamics and propulsive performances. *Physics of Plasmas*, 20 (4):043512, April 2013. doi: 10.1063/1.4798409.

[38] J. D. Burch, D. Han, and S. N. Averkin. Numerical Investigations of 2-D Magnetic Nozzle Effects on Plasma Plumes. In *AIAA Propulsion and Energy 2020 Forum*, AIAA 2020-3643, Virtual, August 2020. American Institute of Aeronautics and Astronautics. doi: 10.2514/6.2020-3643.

VITA

Joshua Daniel Burch was born in 1993 in Las Cruces, New Mexico. In August 2011, he began college at State Fair Community College in Sedalia, Missouri and earned an Associate in Science degree in May 2014. During this time he held multiple leadership positions in the Phi Theta Kappa Honor Society. He continued his undergraduate path at Missouri University of Science and Technology where he earned a Bachelor of Science in Aerospace Engineering degree in December 2018. He became a graduate student under Dr. Han in January 2019, studying computational plasma physics with applications to plasma propulsion. He earned a Master of Science in Aerospace Engineering degree in December 2022. During this time he was active in the Tau Beta Pi engineering honor society and the Missouri S&T Satellite Research Team (M-SAT), where he served in multiple leadership positions including president and chief engineer respectively. He has since begun his professional career at Northrop Grumman Space Systems in Dulles, Virginia.